Cyclic tests on novel steel-concrete-steel sandwich shear walls with boundary CFST columns

Jia-Bao Yan, Yan-Yan Yan, Tao Wang

To cite this version:

Jia-Bao Yan, Yan-Yan Yan, Tao Wang. Cyclic tests on novel steel-concrete-steel sandwich shear walls with boundary CFST columns. Journal of Constructional Steel Research, 2020, 164, pp.105760 -. ⟨10.1016/j.jcsr.2019.105760⟩. ⟨hal-03488576⟩

HAL Id: hal-03488576
https://hal.science/hal-03488576v1

Submitted on 21 Dec 2021

Version of Record: https://www.sciencedirect.com/science/article/pii/S0143974X19309228
Manuscript_c4ec0d3fceb586b58c92afb08d1dc278

Cyclic tests on novel steel-concrete-steel sandwich shear walls with boundary CFST columns

Jia-Bao Yan[a], Yan-Yan Yan[a], Tao Wang[b,*]

[a]*School of Civil Engineering / Key Laboratory of Coast Civil Structure Safety of Ministry of Education, Tianjin University, Tianjin 300350, China*
[b]*Key Laboratory of Earthquake Engineering and Engineering Vibration, Institute of Engineering Mechanics, CEA, Harbin 150080, China*

Abstract: Firstly, this paper proposed a type of steel-concrete-steel (SCS) sandwich composite shear wall with J-hook connectors (SCSSWJ) and boundary concrete-filled-steel-tube (CFST) columns. Five full-scale cyclic tests were performed to study seismic performances of SCSSWJs. The studied parameters were connectors' spacing and axial force ratio. Test results showed that flexure failure occurred to these five SCSSWJs with boundary CFST columns, which is characterized by tensile fracture of boundary steel tube, local buckling in the edge tube and faceplates, and concrete crushing. The test results revealed that increasing the spacing of J-hook connectors from 100 mm to 160 mm and 200 mm firstly slightly improves but then compromised the seismic behaviour of SCSSWJ due to early buckling of steel faceplate; increasing the axial force ratio significantly compromised the seismic behaviours of SCSSWJ. This paper also developed theoretical models to evaluate lateral peak shear resistance of SCSSWJ. The validations proved that the developed models predicted well lateral peak shear resistance of SCSSWJ with boundary CFST columns.

Keywords: Seismic behaviour; sandwich wall; cyclic tests; J-hook connectors; lateral shear resistance; theoretical models.

***Corresponding author**: Tao Wang, E-mail address: wangtao@iem.ac.cn

Nomenclature

A_c=Cross sectional area of concrete

A_s= Cross-sectional area of faceplate

E_e =Dissipated energy for each loading cycle

E_a =Accumulated dissipated energy

H= Height of SCSSWJ

K_0 =Initial stiffness

K_y, K_m, and K_u =Stiffness of SCSSWJ at yield, peak, and ultimate lateral resistance

M_u =Ultimate bending resistance

N= Axial force

N_{cR}= Resultant force of compressive concrete zone

N_s =Resultant compressive force of faceplate

N_T=Resultant compressive force of steel tube in CFST column

N_d =Design axial force

P_y, P_m, and P_u =Yield, peak, and ultimate lateral resistance

P_{ma} =Predicted peak lateral resistance of SCSSWJ

S= Spacing of J-hook

T_s =Resultant tensile force of faceplate

T_T =Resultant tensile force of steel tube in CFST column

W= Width of SCSSWJ

f_c =Concrete compressive strength

f_{cd} =Design compressive strength for concrete

f_y = Yield strength

f_{yc} = Yield strength of steel tube

f_{yd} = Design yield strength

h_c = Thickness of concrete core

n = Axial force ratio

n_d = Design axial force ratio

t_c = Thickness of steel tube

t_s = Thickness of faceplate

t_t = Total cross-sectional depth of SCSSWJ

Δ_y, Δ_m, and Δ_a =Yield, peak, and ultimate displacement

η =Strength degradation ratio

λ_s =Stiffness degradation ratio

μ =Ductility ratio

ω =Compressive strength reduction factor

θ =Drift ratio

θ_u =Ultimate drift ratio

Abbreviations

CFST, concrete filled steel tube; COV, coefficient of variation; MSP, mild steel plate; SCS, Steel-concrete-steel; SCSSS, SCS sandwich structures; SCSSSJ, SCS sandwich structures with J-hook connectors; SCSSW, SCS sandwich wall; SCSSWJ, SCS sandwich wall with J-hooks.

1 Introduction

Steel-concrete-steel (SCS) sandwich structures (SCSSSs) is a type of relative new structure consisting of three layers of materials with a concrete core sandwiched by two layers of external steel skins. This type of structure has been developed for several decades [1], and the extensive advantages perceived from this new structural system include saving labour force and formwork for casting of concrete, avoiding detailing works of reinforcements, providing permanent impermeable membranes by steel faceplates, improved construction efficiency, and promising prefabrication. Due to these advantages, SCSSS shows alternative structural solutions and versatile potential applications in civil, offshore, and nuclear constructions as bridge decking, shear walls in high-rise buildings, offshore decking, undersea oil containers, buried and submerged tunnel linings, liquid and gas retaining structures, protective structures, nuclear shielding wall, and ice-walls [2-3].

Extensive efforts have been made on mechanical connectors to achieve composite actions in SCSSSs, e.g., headed studs [2], angle connectors [4], friction-welded steel bars [5], through bolts [6], laser-welded connectors [7], and double J-hook connectors [8] (See Fig. 1). Previous studies exhibited that SCSSSs with J-hook connectors (SCSSSJs) perform well subjected to static loads [8-10], projectile impact [11], fatigue [12], and occasional blast loads [13]. Due to their advantages and excellent structural performances, SCSSSJ was considered to develop the gravity base Arctic offshore platforms [14-15] as shown in Fig. 2(a). Recently, many new types of structural system have been developed to improve the seismic performance of the high-rise buildings. SCS sandwich shear wall with J-hooks (SCSSWJs) offers one possible solution of these new structural system (see Fig. 2). The proposed structural system could be also used in low-to-medium rise buildings, as alternative to dry lightweight steel systems [16-18]. Moreover, this type of structure can be also used as shielding walls in nuclear power plants. Thus, it can be found that most of these Arctic offshore platforms, high-rise buildings, and nuclear facilities were built in earthquake-prone zones that requires high seismic resistances to prevent environmental pollutions, public safety issues, and losses of property and casualties. Thus, it is important to study seismic behaviours of this novel SCSSWJ.

Due to the novelty of SCSSWJ, previous studies mainly focused on seismic behaviours of SCS sandwich walls (SCSSW) with headed studs and other types of connectors [19-22]. Previous experimental and analytical studies on SCSSWJs concentrated on their static behaviours under out-of-plane shear and bending moment [23-25], punching shear behaviours [26-27], impact behaviours [28-30], blast behaviours [31-32], and fatigue behaviours [33-34]. Studies on seismic behaviours of SCSSWJs are still scared. Therefore, it is necessary to perform corresponding studies on seismic behaviours of SCSSWJ, which would clear the obstacles on applications of this novel SCSSWs in seismic-prone zones.

The present study firstly proposed the SCSSWJ with enhanced concrete-filled-steel-tube (CFST) boundary columns. Cyclic tests were carried out on five full-scale SCSSWJs to study their seismic performances. The investigated parameters were J-hooks' spacing, *S*, and axial force ratio, *n*. With the reported test results, the failure mode, hysteretic load-horizontal displacement behaviours, initial stiffness, load carrying capacity, energy dissipation capacity, and deformation capacity were reported and discussed. Including the tests, the present study also proposed theoretical models to determine the lateral shear resistance of SCSSWJ. At last, conclusions were drawn from the tests and analytical studies.

2 Testing program

2.1 Details of specimens

Five large-scale SCSSWJs in total were prepared, namely SWJ1~SWJ5. Fig. 3 illustrates the main components and construction procedures of SCSSWJ. Each SCSSWJ consists of two boundary CFST columns, a SCS sandwich wall, one base and top endplates. The construction procedures are (1) fabricating J-hooks and welding them to two steel faceplates, (2) preparing CFST columns and welding them to the base plate, (3) welding two steel faceplates to the base plate and CFST boundary columns, (4) preparing the steel skeleton with opening on the top, (5) casting of concrete, and (6) welding the top end plate.

Fig. 4 shows the geometric details of SCSSWJs involved in this study. WBJ1~5 were designed with 109 mm, 1000 mm, and 1830 mm in depth (t_t), width (W), and height (H), respectively. The depth of the concrete core is 100 mm whilst the thickness of the faceplate equals to 4.5 mm. The length of the CFST boundary column equals to 200 mm that is twice its width. Thus, the length of SCSSWJ measures 600 mm. Two variables were considered, i.e., spacing of J-hook connectors (S), and axial force ratio

(n). WBJ1~3 were designed with low, intermediate, and high spacing of J-hook connectors that corresponds to S values of 114, 160, and 200 mm, respectively. Thus, the slenderness ratios (S/t_s) of faceplates in WBJ1~3 are 25.3, 35.6, and 44.4, respectively. Considering the working scenario of SCSSWJ under combined axial compression and lateral loads, low, intermediate and high axial force ratios (n) of 0.55, 0.45, and 0.65 were prepared for WBJ1, WBJ4, and WBJ5, respectively.

WBJ1~5 adopted the same materials for the fabrication of specimens. Grade C35 normal weight concrete (NWS) was used as the core materials in SCSSWJ. Its average compressive strength was 43.3 MPa with a Cov of 0.03. Mild steel plate (MSP) Q235 was used for the boundary CFST column and steel faceplate whilst HPB 335 plain-surface reinforcements were used to produce J-hooks through cold forming. Mechanical properties of these steel materials were obtained through standard tensile tests as specified in GB/T228.1 [35]. For Q235 mild steel plate, its elastic modulus, yield and ultimate strength are 203 GPa, 329.7 and 429.5 MPa, respectively whilst these values for HPB335 are 198 GPa, 343.1 and 497.8 MPa, respectively. Fig. 5 depicts tensile stress versus strain curves of MSP and HPB335 reinforcement.

More details of the prepared specimens WJ1~5 can be found in Table 1.

2.2 Test setup and loading protocol

Fig. 6(a)~(c) depicts the hysteretic test setup of SCSSWJs. All the SCSSWJs were firstly installed to a rigid I-beam support by four arrays of bolts parallel to its four sides. Constant axial compressive force was firstly applied to the SCSSWJ as shown in Fig. 6(a) and (b), which considered the gravity loads acting on the shear wall. The design axial force ratio, n_d, used in this paper is specified as the following [36];

$$n_d = \frac{N_d}{f_{cd}A_c + f_{yd}A_s} \tag{1}$$

where, N_d denotes the design axial compressive force; f_{cd} denotes design concrete compressive strength; A_c is cross-sectional area for concrete; A_s is cross-sectional area for steel. Previous studies showed that the seismic behaviours of SCSSWs were significantly influenced by the axial force ratio [37].

Thus, in this paper, different axial forces of 1397, 1708, and 2018 kN corresponding to axial force ratios of 0.45, 0.55, and 0.65 were applied to WBJ4, WBJ1, and WBJ5 through a hydraulic jack, respectively. Since the lateral restraint needs to be minimized, a sliding support was used at the bottom of hydraulic jack to reduce horizontal frictions between specimens and reaction frames. In order to restrain the out-of-plane displacement, a cladding I-beam frame was used during the testing.

Lateral displacements at different heights of SCSSWJ were measured by five LVDTs as shown in Fig. 6(c). The vertical displacements at the root of the SCSSWJ were monitored by LVDT V1 and V2 as shown in Fig. 6(c). Shear deformations of SCSSWJ were measured by two pair of cross LVDT, namely S1-S4. The detailed layout of these LVDTs is shown in Fig. 6(c). Rosettes and linear strain gauges were used to measure the strains in boundary CFST column and steel faceplate of SCSSWJ as shown in Fig. 6(c). These strain gauges were distributed along four critical cross sections at elevations of 129, 282, 411, 867, and 1323 mm of the SCSSWJ. At each cross section, seven positions were measured along its width, i.e., 0, 100, 236, 500, 764, 900, and 1000 mm from the left edge of the specimen. These installed three-directional rosettes measured the vertical, horizontal, and diagonal shear strains in the steel faceplate. Moreover, the strain distribution along the depth of the cross section can be also estimated. Moreover, the out-of-plane displacement of the SCSSWJ were also monitored by two LVDT (#L1 and L2) during the testing progress as show in Fig. 6(c).

After applying the axial compression force, lateral cyclic loading, provided by a 200-ton horizontal hydraulic actuator, was transferred to the top surface of SCSSWJ through an I-beam (see Fig. 7). The left end of horizontal hydraulic actuator was installed to a reaction wall with the other end connected to the top end of SCSSWJ. Fig. 7 shows the determined loading history in compliance with Chinese code JGJ101-96 [38]. The first three cycles of loadings were force-controlled that equalled to 1/3P_y, 2/3 P_y, and P_y (P_y denotes yielding load of SCSSWJ). After that, the loadings were in displacement-controlled mode, and the amplitudes equal to 1.0, 1.5, 2.0, 2.5… times Δ_y as plotted in Fig. 7. At each loading level, two identical cycles were performed.

3 Test results

3.1 Failure mode and working mechanism

The tests results showed that all the tested SCSSWJs exhibited similar failure patterns and working mechanisms. The working process of SCSSWJ till to failure can be divided into elastic, nonlinear, and recession stages. The observed failure modes at different working stages are illustrated in Fig. 8.

3.1.1 Specimen WBJ1

Slight local buckling took place at final elastic stage at the bottom toe of side plate of boundary CFST column at θ=1.00% (i.e., 88.7% peak resistance) as plotted in Fig. 8(a). Moreover, initiation of local buckling in faceplate was also observed at θ=1.12% as shown in Fig. 8(b). After that, in the nonlinear stage, local buckling gradually developed from boundary column to the middle region of steel faceplate of the SCSSWJ. At θ=1.50%, local buckling occurred to the bottom of faceplate strip locating two rows of J-hooks in SCSSWJ as shown in Fig. 8 (c). Meanwhile, concrete crushing was also observed, and specimen WBJ1 achieved its lateral peak load P_u. During the recession stage, severe local buckling took place in the bottom section of CFST column and faceplate as shown in Fig. 8(d). Tensile fracture at the exterior corner of CFST column, and concrete crushing continued developing (see Fig. 8(d)). Finally, the test was terminated at ultimate drift ratio of 1.89% and failure pattern is shown in Fig. 8(e).

3.1.2 Specimen WBJ2

At the end of first elastic working stage, the slipping sound between steel faceplate and concrete core could be heard at θ=0.75%; meanwhile, local buckling can be also found in the side surface of CFST columns (see Fig. 9(a)). During the second working stage, local buckling continues developing in the faceplate at the bottom toe of SCSSWJ (see Fig. 9(b)). Meanwhile, as shown in Fig. 9(c), the external side surface of CFST column also suffered local buckling. This implies that plastic deformations gradually propagate from external edge to the middle within at the root band of SCSSWJ. At θ=1.25%, tensile fracture in the exterior side plate of CFST column as shown in Fig. 9(d) was observed and WBJ2 achieved its ultimate lateral shear resistance. Finally, at θ=2.00%, the steel faceplate of SCSSWJ and side plate of CFST column locally buckled between first and third horizontal rows (from the bottom) of J-hooks.

3.1.3 Specimen WBJ3

At the final elastic stage (θ=0.6%), steel in the side plate of the CFST column yielded. Then, in nonlinear stage, as θ equals to 0.75%, local buckling occurred to the side surface of CFST column as show in Fig. 10(a). After that, local buckling continued developing from the boundary CFST columns to the middle of SCSSWJ. At θ=1.0%, local region at the bottom of faceplate started to buckle (see Fig. 10(b)). Moreover, local region at the root of side plate in CFST column also buckled [see Fig. 10(c)]. As the drift ratio increased to 1.25%, tensile fracture was observed at the toe of exterior surface in CFST column as shown in Fig. 10(d); meanwhile, WBJ3 achieved its peak resistance. WBJ3 exhibits quite similar failure pattern to WBJ2 that all failed in tensile fracture of the boundary CFST column. Finally, tensile fracture of welding at the edge corner of CFST columns was observed during the recession stage, and concrete crushing could be observed from the opening as shown in Fig. 10(e).

3.1.4 WBJ4

The elastic behaviour of WBJ4 terminated at θ=1.12% when local buckling in the side surface of CFST column took place [see Fig. 10(a)]. This local buckling became more transparent at θ=1.37% [see Fig. 10(b)]. After that, local buckling regions gradually propagated from the edge column to the middle at the bottom strip of specimen, and this whole strip fully locally buckled as θ equals to 1.52% as shown in Fig. 10(c). Tensile fracture of the CFST column was observed at θ=1.65%; meanwhile, WBJ4 achieved it lateral peak resistance. Local buckling further developed and became more severe, and the testing terminated at θ=2.10%.

3.1.5 WBJ5

The elastic working stage of WBJ5 was terminated at about θ=0.70% when the steel in the CFST boundary column yielded. In nonlinear stage, the local buckling of longer side faceplate of CFST column took place at θ=0.87% as shown in Fig. 12(a). Followed, local buckling occurred to the faceplate in its middle bottom region at θ=1.12% as shown in Fig. 12(b). Meanwhile, severe local buckling continued developing in all external surfaces of boundary CFST column at θ=1.37% [see Fig. 12(c)]. Meanwhile, the local buckling developed very fast within the strip between the bottom 2nd and 3rd row of connectors as shown in Fig. 12(d). Finally, local buckling of faceplate and concrete crushing occurred to WBJ5 at θ=1.50% [see Fig. 12(d)], and the specimen suddenly lost its load carrying capacity. Meanwhile, tensile fracture of the weld at corner of CFST column was also observed, and severe local buckling was observed at the bottom of WBJ5 as shown in Fig. 12(e).

3.2 Load-displacement relationship

Hysteretic load-displacement curves of WBJ1~5 are plotted in Fig. 13. This figure also identifies occurrences of different events during the cyclic testing that include (1) steel yielding, (2) local buckling of longer plate in CFST column, (3) local buckling of exterior shorter plate in CFST column, (4) local buckling of steel faceplate in SCSSWJ, (5) tensile facture of steel plate in CFST, (6) tensile fracture of welding at corner, and (7) concrete crushing. These five figures shows that (1) before steel yielding of the CFST column, all the specimens behave elastically; (2) local buckling in the CFST column occurred after the steel yielding, but prior to buckling of faceplate in SCSSWJ; (3) tensile fracture of CFST column or local buckling of faceplate occurred as SCSSWJ achieved its lateral peak shear resistance.

As shown in Fig. 13, all these hysteretic curves are in a ductile manner without evident pinching effect that implies the flexural failure mode occurred to most of the specimens. This figure also shows that before yielding of CFST column all the hysteretic curves exhibit elastic behaviour with small residual drift less than 0.001. After that, the lateral load resistance increases in a nonlinear manner with decreasing stiffness. As the drift ratio increases to 0.01 (the drift ratio limit under rare earthquake for RC shear wall as specified in GB50011-2010), the residual drift ratios for most of SCSSWJs are about 0.002. After achieving their peak resistances, the hysteretic curves for WBJ1~5 exhibited rapid reduction due to concrete crushing or local buckling of faceplate. The residual drift ratios increase with increasing loading cycles.

The displacement in Fig. 13 mainly consists of components produced by flexural bending and lateral shear force. Fig. 14 compares the shear deformation with the total deformation for WBJ1 and WBJ4. The shear deformation of the SCSSWJ can be obtained as the following;

$$\Delta_s = \frac{D}{2W}\left[\left(\Delta_{S2}-\Delta_{S1}\right)+\left(\Delta_{S4}-\Delta_{S3}\right)\right] \tag{2}$$

where, D denotes the diagonal distance of the two measuring points by LVDT S1~4 as shown in Fig. 6(c); W denotes width of the SCSSWJ; $\Delta_{S1}, \Delta_{S2}, \Delta_{S3}$, and Δ_{S4} denote diagonal displacements measured by LVDT S1, S2, S3, and S4 (see Fig. 6c), respectively.

From Fig. 14, it can be seen that shear deformation only occupies less than 10% of total deformation that implies the flexural bending governs the structural deformation of SCSSWJ during the test.

The hysteretic curves also show that increasing the spacing of J-hooks influences the hysteretic loops. Increases the S value from 114 to 160 mm results in earlier steel yielding of CFST, but has marginal influence on the shape of hysteretic loops. However, as S is beyond 160 mm and less than 200 mm, the shape of hysteretic load-displacement curves is significantly affected and becomes less plump, which implies the reduced energy dissipation capacity. Fig. 13 also shows that the hysteretic loops of SCSSWJ is obviously influenced by the axial force ratio. When the n_d increases from 0.45 to 0.55 and 0.65 pinching effect becomes more obvious, and the loops become less plump that implies reduced energy dissipation capacity. Moreover, the hysteretic loops become sharper that is especially obvious in the hysteretic loops of specimen WBJ6 with n_d of 0.65.

3.3 Skeleton curves, characteristic deformations and resistances

Fig. 15 depicts the skeleton hysteretic load-displacement curves of WBJ1~5. The yield load (P_y), peak load (P_m), and ultimate load (P_u) as well as their corresponding displacements Δ_y, Δ_m, and Δ_u are determined by the energy method as introduced in Fig. 16. Table 2 lists these determined values. Fig. 17 plots influences of S and n_d on strengths and deformation capacity of SCSSWJ. As shown in this figure, increasing S value from 114 to 160 and 200 mm results in 0% and 14% decreases in yield load P_y and -7% and 11% decreases in peak load P_m (negative decrease means increase). However, the initial stiffness K_0 was only decreased by -2% and 4% when S value is enlarged from 114 to 160 and 200 mm, which implies the marginal influence of S on initial stiffness. This is because increasing S actually enlarges the slenderness ratios of faceplate in SCSSWJ which resulted in reduced cross-sectional bending resistance and thus the lateral shear resistance of shear wall. However, the spacing of J-hooks has quite limited influence on the initial stiffness of SCSSWJ. Fig. 17(b) shows that as S value increases from 114 to 160 and 200 mm, the Δ_u (or Δ_y) is firstly slightly increased by 11% (or 1%) and then decreased by 11% (or 17%). The specimen with S value of 160 mm offers the best ultimate displacement capacity. However, as S

increases, the ultimate displacement will be compromised due to local buckling of the steel faceplates.

As reflected in Fig. 17(c), as n_d increases from 0.45 to 0.55 and 0.65, the yield load P_y receives its increases of 6% and 10% whilst P_m is increased by 7% and 13%, respectively. However, the initial stiffness K_0 is significantly increased by 10% and 38% as n_d increases from 0.45 to 0.55 and 0.65, respectively. This is because the axial force ratio changes the neutral axis position that results in different moment of inertia of the cross section as well as the lateral stiffness. Moreover, as shown in Fig. 17(d), the increasing axial force ratio significantly reduces the ultimate displacement of the SCSSWJ. As n_d increases from 0.45 to 0.55 and 0.65, the ultimate displacement Δ_u is reduced by 8% and 28%, respectively.

3.4 Strength degradation

The strength degradation is a key index to evaluate the structural behaviour of SCSSWJ under cyclic loading, and it is defined as the following [19, 37];

$$\eta_i = \frac{P_i^n}{P_i^1} \tag{3}$$

where, η_i is the strength degradation ratio; P_i^1 and P_i^n denotes ultimate load of the first and n^{th} cycle at loading level i, respectively.

Fig. 18 depicts the η_i ratios versus different displacement loading level curves. It shows that as the lateral displacement is less than 24 mm the strength degradation ratios of WBJ1~5 are within 0.95~1.0 that implies slight strength degradation, and during the increase of drift from 24 to 30 mm the value of η_i rapidly decreases to about 0.7 due to concrete crushing and faceplate's local buckling of. As the displacement is beyond 15 mm, the specimen WBJ5 with the largest n_{d} ratio and WBJ3 with the largest spacing of J-hook exhibit rapid decreases to about 0.8 as the displacement equals to about 30 mm due to local buckling of CFST column and steel faceplate. For specimens WBJ2 with intermediate S value of 160 mm and WBJ4 with intermediate n_{d} ratio, they exhibit close strength degradation behaviours to WBJ1.

3.5 Stiffness degradation

The lateral stiffness of SCSSWJ is defined as follows [21];

$$K_i = \frac{\sum_{j=1}^{n} P_i^j}{\sum_{j=1}^{n} \Delta_i^j} \tag{4}$$

where, K_i denotes lateral stiffness at i^{th} displacement loading level; P_i^j is ultimate strength of j^{th} cycle at i^{th} displacement; Δ_i^j denotes displacement at P_i^j; n denotes number of cycles.

Fig. 19 plots stiffness versus displacement level curves for WBJ1~5. Table 2 tabulates theose determined K_{y}, K_{m}, and K_{u} values corresponding to yield, peak, and ultimate loads. These figure and table show that (1) specimen WBJ5 exhibits faster stiffness degradation than the rest specimens due to its largest axial force ratio; (2) WBJ3 exhibits more rapid decrease in the lateral stiffness than WBJ1 due to larger S value in WBJ3; (3) specimen WBJ1, WBJ2, and WBJ4 exhibit close lateral stiffness vs. displacement behaviours, i.e., the lateral stiffness gradually decreased from 50 to 20 kN/mm; (4) the average K_y/K_0, K_m/K_0, and K_u/K_0 ratios are about 0.70, 0.52, and 0.40, respectively.

3.6 Deformation capacity and ductility ratio

Using the method in Fig. 16, displacements Δ_y, Δ_m, and Δ_u corresponding to P_y, P_m, and P_u are determined by the energy method as listed in Table 2. Moreover, Table 2 also lists the ultimate drift ratios θ_u. The ductility ratio describing deformation capacity of SCSSWJ under lateral loads is specified as the following;

$$\mu = \frac{\Delta_u}{\Delta_y} \tag{5}$$

All these calculated ductility ratios are listed in Table 2. Fig. 20 shows the influences of S and n_d on ductility ratios of SCSSWJ.

From this table and figure, it can be found that;

(1) The average θ_u value is about 1.7%. The ultimate drift ratio firstly increases from 1.74% to 1.94% and then decreases to 1.55% when S is enlarged from 114 to 160 and 200 mm. This implies increasing the S value from 114 to 160 mm has positive influence on its ultimate drift ratio.

(2) Increasing n_d from 0.45 to 0.55 and 0.65 reduces the average θ_u value from 1.88 to 1.74 and 1.35, which implies the axial force ratio has negative influences on its ultimate deformation capacity.

(3) The average ductility ratio for five tests is about 1.65 and most of the ductility ratios are within 1.39~1.85.

(4) Increasing S value from 114 to 160 and 200 mm averagely increases the μ value by 10% and 6%, respectively. This implies that increasing spacing of J-hook improved the ductility of the SCSSWJ.

(5) Increasing n_d from 0.45 to 0.55 and 0.65 decreases the μ value of SCSSWJ from 1.79 to 1.57 and 1.47 that corresponds to 12% and 18% reductions, respectively.

3.7 Energy dissipation capacity

Following the definition in Fig. 21, Fig. 22 depicts the dissipated energy for each cycle, E_e, and accumulated dissipated energy, E_a. This figure shows that the energy dissipation capacity of SCSSWJ increases as the lateral displacement loading increases. As lateral drift is less than 12 mm (θ_e=0.6%), the E_e and E_a values are marginal small that means elastic behaviour of SCSSWJs. Once the lateral drift is beyond 12 mm, the energy dissipation capacities of WBJ1 and WBJ5 start to increase rapidly. The energy dissipation capacities of WBJ2~4 exhibit rapid increases as the lateral drift is beyond 15 mm.

Fig. 23 depicts the relationship between lateral drift and equivalent viscous damping ratios of WBJ1~5. It shows that the equivalent damping ratio firstly remains almost constant at about 0.3, and then increase rapidly at different drift ratios that vary with different specimens. These rapid increases in the equivalent viscous damping ratios were mainly due to yielding of the steel CFST column and steel faceplate in

SCSSWJs.

3.8 Strains

Cyclic load-strain curves in CFST columns at the most critical position of SCSSWJ are plotted in Fig. 24. The positive and negative values of strains in Fig. 23 denote tensile and compressive stress state, respectively. This figure shows that the compressive strains exhibit obvious faster increase than the tensile strains, e.g., the compressive and tensile strains at the peak lateral load for WBJ2 right edge are 0.020 and 0.0018, respectively. This biased distribution of the strain at the compression portion of the cross section was mainly due to local buckling of steel tube in CFST column and crushing of infilled concrete core.

Fig. 25 plots vertical strain profiles corresponding to different loadings at the bottom of specimen, e.g., $0.25P_y$, $0.5\ P_y$, $0.75\ P_y$, P_y and peak load P_m for representative specimens WBJ1 and WBJ2. These two figures show that the strain distribution profiles still satisfy the plane section assumption from the loading initiation to the peak load of SCSSWJ.

4 Theoretical models on lateral peak shear resistance of SCSSWJ

4.1 Theoretical models on lateral peak shear resistance of SCSSWJ

Test results revealed the flexural failure of all SCSSWJs, which implies P_m of this novel sandwich shear wall is determined by its ultimate bending resistance of SCSSWJ's cross section. The following assumptions were made to perform the analysis on ultimate bending resistance of the SCSSWJ with boundary CFST column:

(1) plane section assumption still works; (2) concrete tensile strength is neglected; (3) local buckling governs the compressive resistance of and steel faceplate of SCSSWJ and steel tube in CFST column.

Strains and internal forces in the cross section of SCSSWJ are plotted in Fig. 26. Since there is only one unknown variable, i.e., neutral axis position, it can be solved through the equilibrium of resultant force of the cross section equalling to external applied axial compression as the following;

$$N = N_{cR} + N_T + N_s - T_T - T_s \tag{6}$$

$$N_{cR} = (\gamma x)(\omega f_c)h_c \tag{7}$$

$$N_T = \min(\sigma_{cr}, f_y)\left[h_c t_c + 2(W_c + t_c)t_c\right] + f_{yc} h_c t_c \tag{8}$$

$$N_s = 2\min(\sigma_{cr}, f_y)(x - W_c - t_c)t_s \tag{9}$$

$$T_T = (h_c + 3t_c + W_c)t_c f_y \tag{10}$$

$$T_s = 2t_s(W - x - W_c - 0.5t_c)f_y \tag{11}$$

where, N is the applied axial force; N_{cR} is internal compressive force of concrete; N_{T} denotes compressive force of steel tube in CFST column; N_{s} denotes internal compressive force of faceplate; T_{T} is internal tensile force contributed by the steel tube of CFST column in tensile zone of cross section; T_{S} is internal tensile force of faceplate; h_{c} is the depth of core; t_{c} is the thickness of tube in CFST column; t_{s} is thickness of faceplate in SCSSWJ; W is width of SCSSWJ; W_{c} denotes width of the CFST column; γ is the reduction factor for x as specified in Eurocode 2 [39]; ω is the compressive strength reduction factor as specified in Eurocode 2 [39]; $\sigma_{cr} = \min\left[\frac{\pi^2 E_s}{12K^2\left(S/t_s\right)^2}, f_y\right]$; *S* is connector's spacing; *K* is coefficient for boundary condition and herein is adopted as 0.6; f_y is yield strength; f_{yc} denotes yield strength of steel tube in CFST column.

With the solved neutral axis potion *x*, the cross-sectional bending resistance of SCSSWJ, M_u, can be determined as follows;

$$\begin{aligned} M_u &= 0.5N_{cR}\left(W-\lambda x\right)+0.5N_T\left(W-W_c\right)+0.5N_s\left(W-x-W_c\right) \\ &+0.5T_T\left(W-W_c\right)+0.5T_s(x-W_c) \end{aligned} \tag{12}$$

The ultimate lateral shear resistance of SCSSWJ with boundary CFST column can be calculated as follows;

$$P_{ma} = M_u / H \tag{13}$$

where, *H* is the height of SCSSWJ.

4.2 Validations and discussions

The predicted lateral peak shear resistances for WBJ1~5 are compared with those experimental values in Table 2. Fig. 27 compares the predicted lateral peak resistances of SCSSWJ with corresponding test results. These table and figure show that the developed analytical models offer an average 28% estimation with a Cov of 7% for ten cases for the lateral peak shear resistance of SCSSWJ. The conservative predictions by the proposed analytical models may be due to ignoring strength hardening of the steel faceplate and steel tube in CFST since tensile fracture occurred to the steel tube of CFST column. Since limited validations of the proposed model were performed, and they still require further more validations.

5 Conclusions

This study firstly reported five full-scale cyclic tests on SCSSWJ with boundary CFST columns. The studied key parameters were connectors' spacing and axial force ratio. Theoretical models were also developed to predict the lateral peak shear resistance of SCSSWJ. These experimental and analytical studies support the following conclusions;

(1) Flexural failure occurred ot SCSSWJ with boundary elements that is characterized by yielding of steel tube and faceplate in SCSSWJ and concrete crushing.

(2) As the connectors' spacing is less than 160 mm, increasing S has positive influence on energy dissipation capacity, lateral peak shear resistance, deformation capacity, and ductility of SCSSWJ. However, as S is beyond 160 mm till 200 mm, increasing S reduces energy dissipation capacity, lateral peak shear resistance, deformation capacity, and ductility of SCSSWJ. However, increasing S did not affect the initial stiffness of SCSSWJ.

(3) Increasing n_d of SCSSWJ from 0.45 to 0.65 results in significant reductions of energy dissipation capacity, ductility, and deformation capacity, but increases the initial stiffness and lateral peak shear resistance of SCSSWJ. This increasing axial force ratio also accelerated the stiffness degradation and strength degradation of the SCSSWJ subjected to horizontal cyclic loading.

(4) The premature local buckling in the tube and steel tube and faceplate reduces the energy dissipation and lateral peak shear resistance of SCSSWJ. The layout of J-hook connectors required further optimization that influences seismic behaviours of SCSSWJ.

(5) Theoretical models have been proposed for lateral shear resistance of SCSSWJ with boundary CFST columns. The validations proved that these models averagely underestimated the lateral peak shear resistance of SCSSWJ by 28%. These underestimations were mainly due to ignoring strength hardening of the steel materials. However, considering the limited validation further validations are still necessary.

ACKNOWLEDGMENT

The authors would like to acknowledge the research grant 51608358 received from National Natural Science Foundation of China and Peiyang Scholar Foundation (grant no. 2019XRX-0026) under Reserved Academic Program from Tianjin University for the works reported herein. The authors gratefully express their gratitude for the financial supports.

References

[1] Montague P. A simple composite construction for cylindrical shells subjected to external pressure. J. Mech. Eng. Sci. 1975; 17: 105-113.
[2] Wright HD, Oduyemi TOS. Partial interaction analysis of double skin composite beams. J. Construct. Steel Research 1991; 19: 253-283.
[3] Yan JB, Liu XM, Liew JYR, Qian X, Zhang MH. Steel-concrete-steel sandwich system in Arctic offshore structures: materials, experiments, and design. Materials & Design 2016; 91: 111-121.
[4] Malik N, Mchida A, Mutsuyoshi H, Makabe T. Steel-concrete sandwich members without shear reinforcement, Transaction of the Japan Concrete Institute 1993; 15(2): 527-534.
[5] Xie M, Foundoukos N, and Chapman JC. Experimental and numerical investigation on the shear behaviour of friction-welded bar–plate connections embedded in concrete. J. Construct. Steel Research 2004; 61: 625–649.

[6] Ji X, Jiang F, Qian J. Seismic behaviour of steel tube-double steel plate-concrete composite walls: Experimental tests. Journal of Constructional Steel Research 2013; 86: 17-30.

[7] Leekitwattana M, Boyd SW, Shenoi RA. Evaluation of the transverse shear stiffness of a steel bi-directional corrugated-strip-core sandwich beam. Journal of Constructional Steel Research 2011; 67(2): 248-254.

[8] Yan JB, Liew JYR, Zhang MH, Sohel KMA. Experimental and analytical study on ultimate strength behaviour of steel-concrete-steel sandwich composite beam structures. Materials and Structures 2015; 48(5): 1523-1544.

[9] Liew JYR and Sohel KMA. Lightweight steel-concrete-steel sandwich system with J-hook connectors. Engineering structures 2009; 31: 1166-1178.

[10] Sohel KMA and Liew JYR. Steel–Concrete–Steel sandwich slabs with lightweight core -Static performance. Engineering Structures 2011; 33(3): 981-992.

[11] Sohel KMA, Liew JYR and Koh CG. Numerical modelling of lightweight Steel Concrete Steel sandwich composite beams subjected to impact. Thin-Walled Structures 2015; 94: 135-146.

[12] Dai XX, Liew JYR. Fatigue performance of lightweight steel–concrete–steel sandwich systems. J. Constr. Steel. Res. 2010; 66(2): 256–276.

[13] Liew JYR, Wang T. Novel Steel Concrete Steel Sandwich Composite Plates Subject to Impact and Blast Load. Advances in Structural Engineering 2011; 14(4): 673-687.

[14] Marshall PW, Palmer AC, Liew JYR, Wang TY, Thein MKW. Bond Enhancement for sandwich shell ice wall, in: International conference and exhibition on performance of ships and structures in ice, 20–23 September, Alaska, USA, 2010.

[15] Yan JB, Liew JYR. Design and behavior of steel–concrete–steel sandwich plates subject to concentrated loads. Compos. Struct. 150 (2016) 139–152.

[16] Fiorino L, Terracciano MT, Landolfo R. Experimental investigation of seismic behaviour of low dissipative CFS strap-braced stud walls. Journal of Constructional Steel Research 2016; 127: 92-107.

[17] Mohebbi S, Mirghaderi SR, Farahbod F, Sabbagh AB, Torabian S. Experiments on seismic behaviour of steel sheathed cold-formed steel shear walls cladded by gypsum and fiber cement boards. Thin-Walled Struct. 2016; 104: 238–247.

[18] Fiorino L, Macillo V, Landolfo R. 2017. Shake table tests of a full-scale two-story sheathing-braced cold-formed steel building. Engineering Structures 2017; 151: 633–647.

[19] Ji X, Cheng X, Jia X, Varma AH. Cyclic in-plane shear behaviour of double skin composite shear walls in high-rise buildings. J. Struct. Eng. ASCE 2017; 143(6): 04017025.

[20] Nie JG, Qin K, Cai CS. Seismic behavior of connections composed of CFSSTCs and steel–concrete composite beams-experimental study. J Constr Steel Res 2008; 64(10):1178–91.

[21] Hu HS, Nie JG, Fan JS, Tao MX, Wang YH, Li SY. Seismic behaviour of CFST-enhanced steel plate-reinforced concrete shear walls. Journal of Constructional Steel Research 2016; 119: 176-189.

[22] Epackachi S, Nguye NG, Kurt EG, Whittaker AS. In-plane seismic behaviour of rectangular steel-plate composite wall piers. J. Struct. Eng. ASCE 2015; 141(7): 04014176.

[23] Liew JYR and Sohel KAM. Lightweight steel-concrete-steel sandwich system with J-hook connectors. Engineering structures 2009; 31: 1166-1178.

[24] Sohel KMA, Liew JYR, Yan JB, Zhang MH, Chia KS. Behavior of Steel–Concrete–Steel sandwich structures with lightweight cement composite and novel shear connectors. Composite Structures 2012; 94(12): 3500-3509.

[25] Yan JB, Liew JYR, Zhang MH, Sohel KMA. Experimental and analytical study on ultimate strength behaviour of steel-concrete-steel sandwich composite beam structures. Materials and Structures 2015; 48(5): 1523-1544.

[26] Sohel KMA and Liew JYR. Steel–Concrete–Steel sandwich slabs with lightweight core -Static performance. Engineering Structures 2011; 33(3): 981-992.

[27] Yan JB, Liew JYR, Zhang MH, Li ZX. Punching shear resistance of steel-concrete-steel sandwich composite shell structure. Engineering Structures 2016; 117(0): 470-485.

[28] Sohel KMA. Impact behaviour of Steel-Composite sandwich beams. PhD. Eng. Thesis, National University of Singapore. 2008.

[29] Sohel KMA, Liew JYR and Koh CG. Numerical modelling of lightweight Steel Concrete Steel sandwich composite beams subjected to impact. Thin-Walled Structures 2015; 94: 135-146.

[30] Sohel KMA, Liew JYR. Behavior of steel–concrete–steel sandwich slabs subject to impact load. J. Constr. Steel. Res. 2014; 100:163-175.

[31] Kang KW. Blast resistance of steel-concrete composite structures. PhD thesis, Department of Civil and Environmental Engineering, National University of Singapore; 2012.

[32] Liew, J Y R and T Wang. Novel Steel Concrete Steel Sandwich Composite Plates Subject to Impact and Blast Load. Advances in Structural Engineering 2011; 14(4): 673-687.

[33] Dai XX. Fatigue analysis and design of steel-concrete-steel sandwich composite structures. National University of Singapore, PhD thesis, 2009.

[34] Dai XX, Liew JYR. Fatigue performance of lightweight steel–concrete–steel sandwich systems. J. Constr. Steel. Res. 2010; 66(2): 256–276.

[35] GB/T228.1—2010 Metallic materials: tensile testing. Beijing: China Planning Press, 2010 (in Chinese)).

[36] JGJ 3-2010. Technical specification for concrete structures of tall building (JGJ3-2011). Beijing: China Ministry of Construction, 2011 (in Chinese).

[37] Yan JB, Li ZX, Wang Tao. Seismic behaviour of double skin composite shear walls with overlapped headed studs. Construction and Building Materials 2018; 191: 590-607.

[38] JGJ101-96. Specification of testing methods for earthquake resistant building. China Planning Press, Beijing, 1997.

[39] Eurocode 2, Design of Concrete Structures — Part 1–1: General Rules and Rules for Buildings, BS EN 1992-1-1, 2004.

Table 1 Details of SCSSWJ for cyclic tests

Item	Aspect ratio	S (mm)	t_s (mm)	S/t_s ratio	Axial force (kN)	n_d
WBJ1	2	114	4.5	25.3	1708	0.55
WBJ2	2	160	4.5	35.6	1708	0.55
WBJ3	2	200	4.5	44.4	1708	0.55
WBJ4	2	114	4.5	25.3	1397	0.45
WBJ5	2	114	4.5	25.3	2018	0.65

S denotes spacing of J-hook; t_s denotes thickness of steel faceplate; S/t denotes slenderness ratio; n_d denotes axial force ratio.

Table 2 Test results of SCSSWJ under horizontal cyclic loads

Item	Load Direction	Δ_y (mm)	P_y (kN)	Δ_m (mm)	P_m (kN)	Δ_u (mm)	θ_u (%)	P_u (kN)	$\mu = \frac{\Delta_u}{\Delta_y}$
(1)	(2)	(3)	(4)	(5)	(6)	(7)	(8)	(9)	(7)/(3)
WBJ1	(-)	23.7	811.4	30.0	881.4	34.6	1.73	749.2	1.46
	(+)	20.9	761.4	32.8	868.9	34.9	1.75	738.6	1.67
WBJ2	(-)	20.4	776.7	30.8	953.6	37.7	1.89	810.6	1.85
	(+)	24.8	791.6	36.2	910.7	39.4	1.97	774.1	1.59
WBJ3	(-)	16.3	632.0	22.3	735.6	27.4	1.37	625.2	1.68
	(+)	20.9	717.2	25.5	828.9	34.5	1.73	704.6	1.65
WBJ4	(-)	19.0	737.8	31.7	844.6	35.2	1.76	717.9	1.85
	(+)	23.2	747.4	33.1	793.1	40.0	2.00	674.1	1.72

WBJ5	(-)	16.9	824.3	24.9	914.9	26.2	1.31	777.7	1.55
	(+)	19.9	814.6	25.3	930.7	27.6	1.38	791.1	1.39

Table 2 continued

Item	Load Direction	K_0 (kN/mm)	K_y (kN/mm)	K_y/K_0	K_m (kN/mm)	K_m/K_0	K_u (kN/mm)	K_u/K_0	P_{ma} (kN)	P_m/P_{ma}
(1)	(2)	(3)	(4)	(4)/(3)	(6)	(6)/(3)	(8)	(8)/(3)	(10)	(11)
WBJ1	(-)	52.7	34.2	0.65	29.2	0.55	21.7	0.41	690.1	1.28
	(+)	52.6	36.4	0.69	25.9	0.49	21.2	0.40	690.1	1.26
WBJ2	(-)	52.5	38.1	0.73	30.6	0.58	19.9	0.38	677.2	1.41
	(+)	54.9	31.9	0.58	24.4	0.44	19.7	0.36	677.2	1.34
WBJ3	(-)	52.6	38.7	0.74	27.4	0.52	22.7	0.43	651.3	1.13
	(+)	48.5	34.4	0.71	26.1	0.54	20.4	0.42	651.3	1.27
WBJ4	(-)	48.4	38.8	0.80	26.0	0.54	20.4	0.42	688.9	1.23
	(+)	47.4	32.2	0.68	23.4	0.49	16.8	0.35	688.9	1.15
WBJ5	(-)	68.1	48.8	0.71	35.1	0.52	29.7	0.43	686.0	1.33
	(+)	64.3	40.9	0.64	36.5	0.57	28.6	0.44	686.0	1.36
Mean										1.28
Cov										0.07

Δ_y, Δ_m, and Δ_u denote yield, peak, and ultimate displacement of SCSSWJ, respectively; P_y, P_m, and P_u denote strengths of SCSSWJ corresponding to Δ_y, Δ_m, and Δ_u, respectively; P_{ma} denotes predicted peak load; K_0 denotes cyclic initial stiffness; μ denotes displacement ductility ratio.

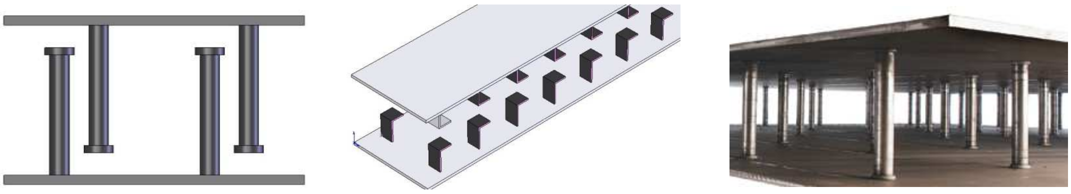

(a) Headed studs (b) Angle connectors (c) Friction welded steel bars

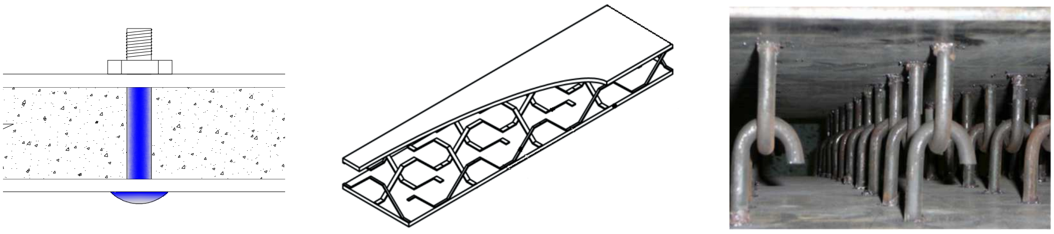

(d) Through bolt connectors (e) Corrugated-strip connectors (f) J-hook connectors

Fig. 1 Different types of mechanical connector in SCS sandwich structures [8]

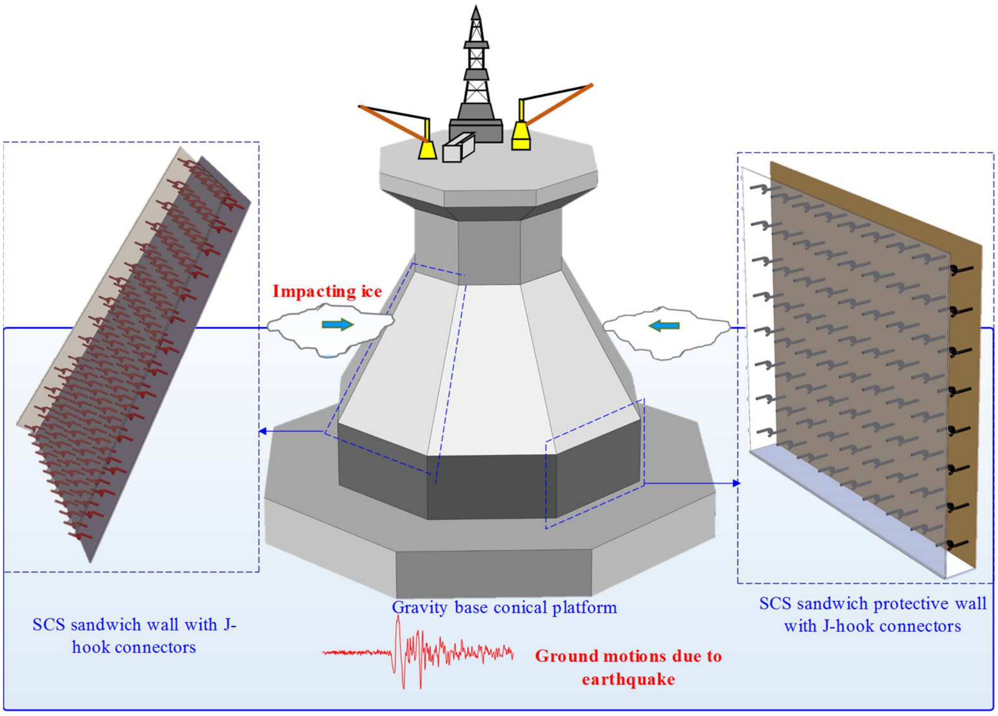

(a) Ice-resistant wall in the Arctic offshore platforms

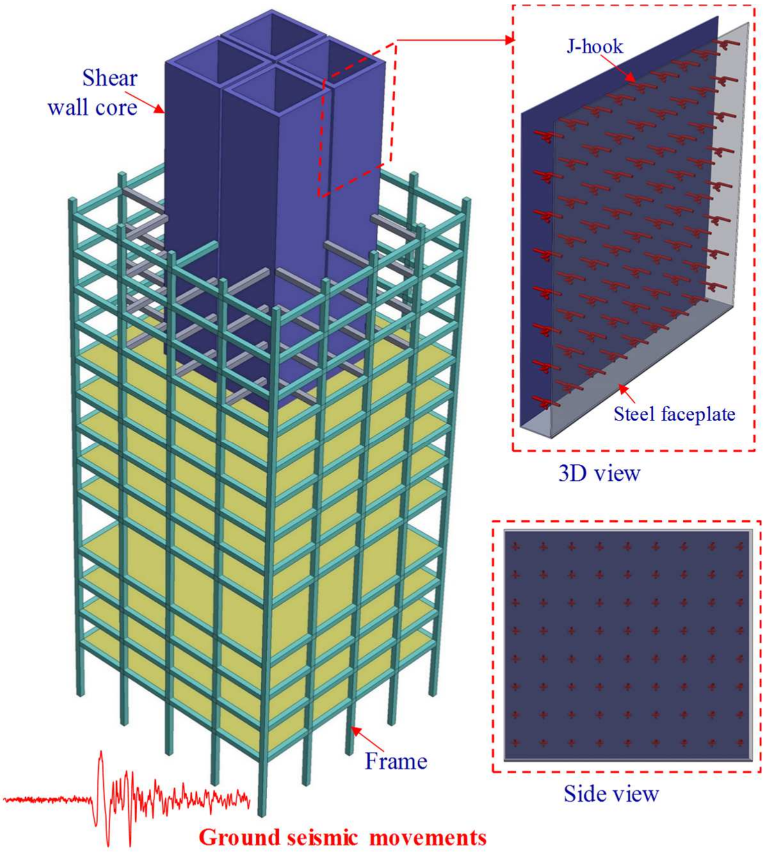

(b) SCS sandwich shear wall with J-hook connectors

Fig. 2 Applications of SCS sandwich walls

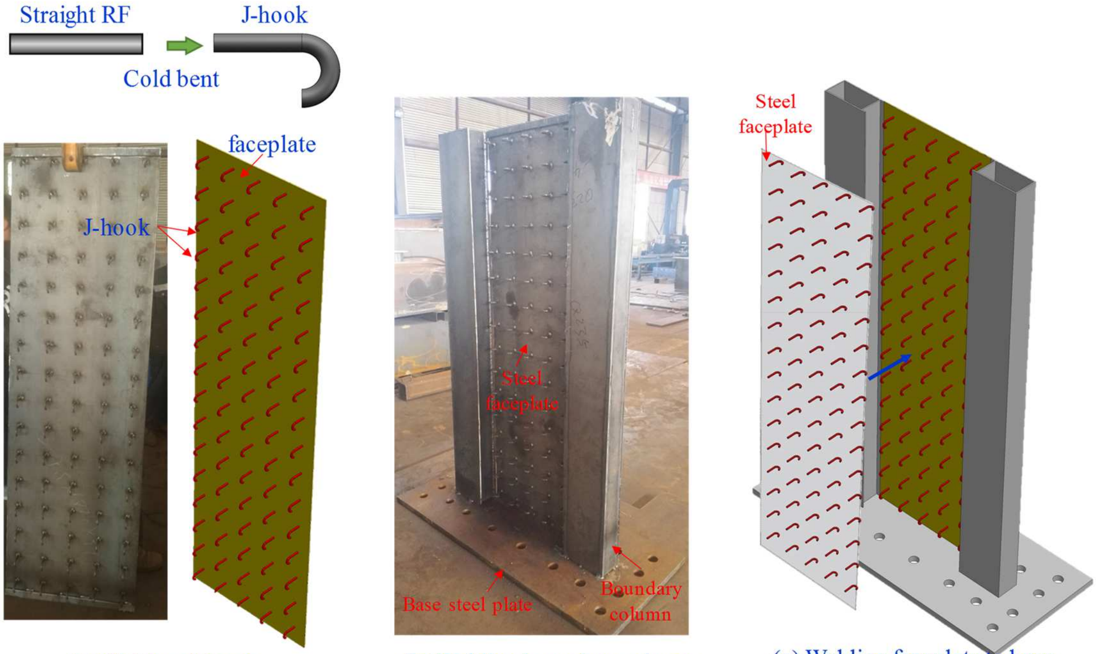

(a) Welding J-hook connectors to steel faceplate

(b) Welding boundary column and faceplate to base plate

(c) Welding faceplate to base plate and boundary column

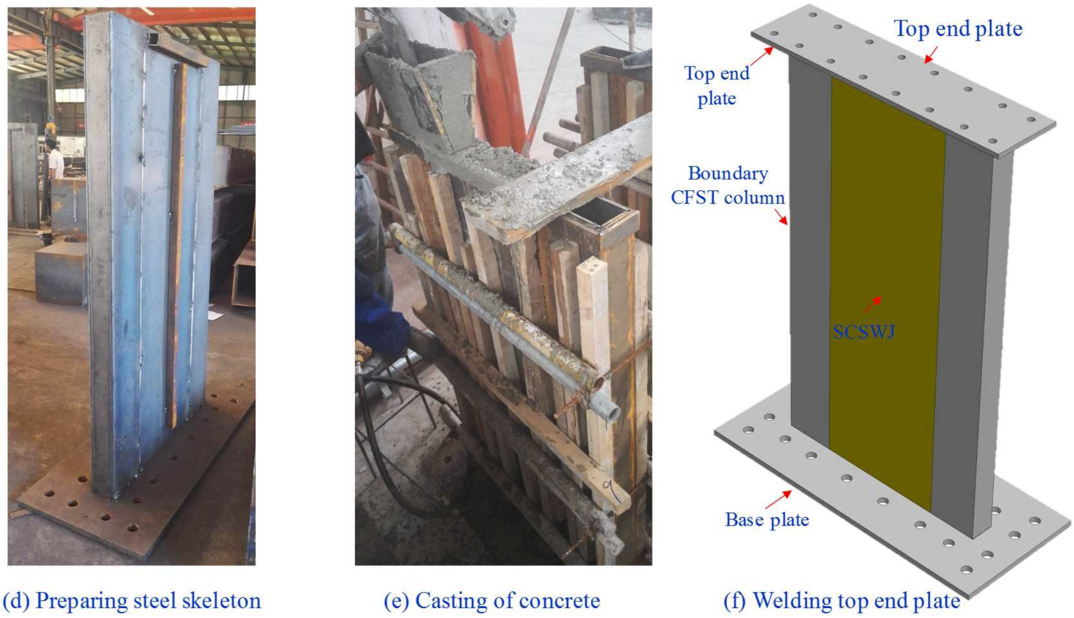

(d) Preparing steel skeleton (e) Casting of concrete (f) Welding top end plate

Fig. 3 Fabrication procedures of SCSSWJ

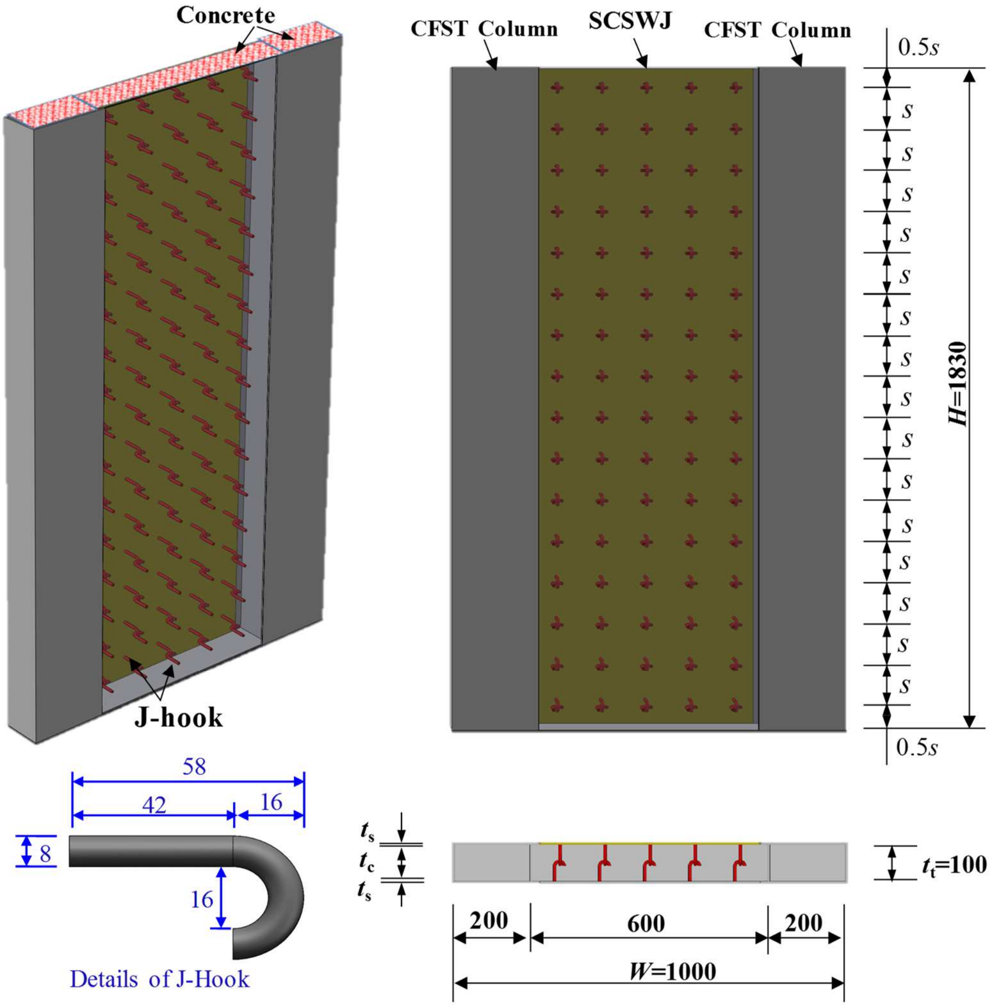

Fig. 4 Geometric details of SCSSWJ (unit: mm)

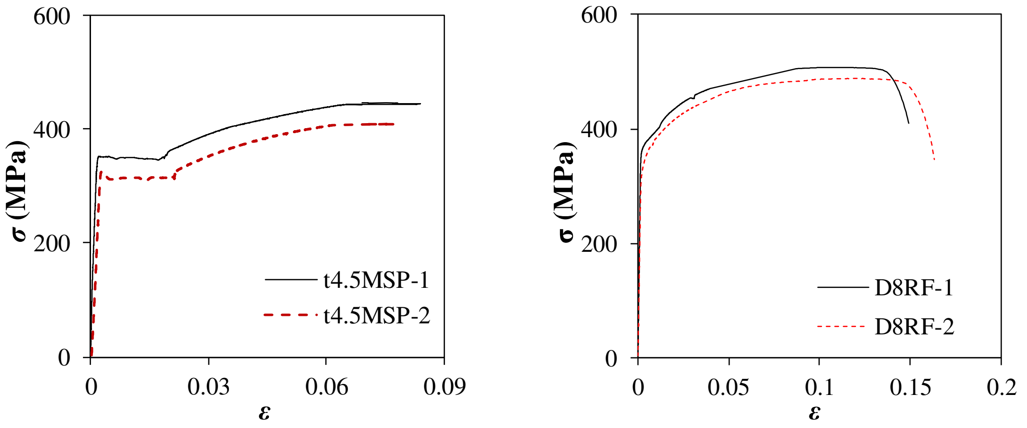

(a) Tensile stress-strain curves of 4.5mm MSP

(b) Tensile stress-strain curves of Φ8 steel reinforcement

Fig. 5 Tensile stress-strain curves of Q235 MSP and HPB335 and steel reinforcement

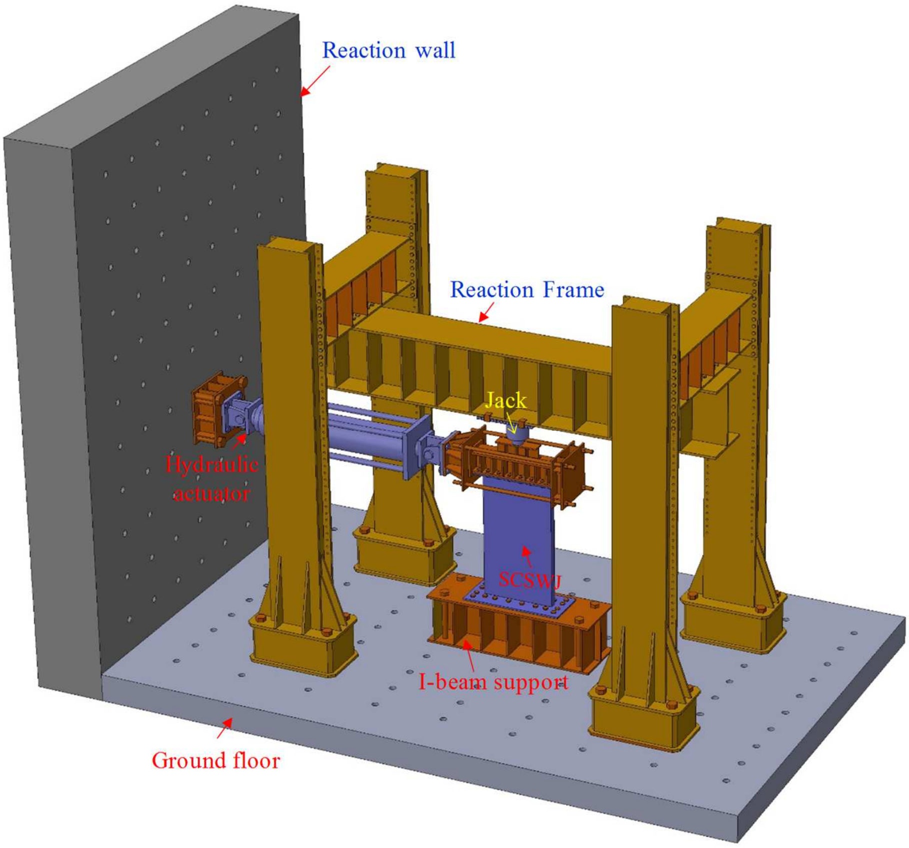

(a) 3D view of test setup

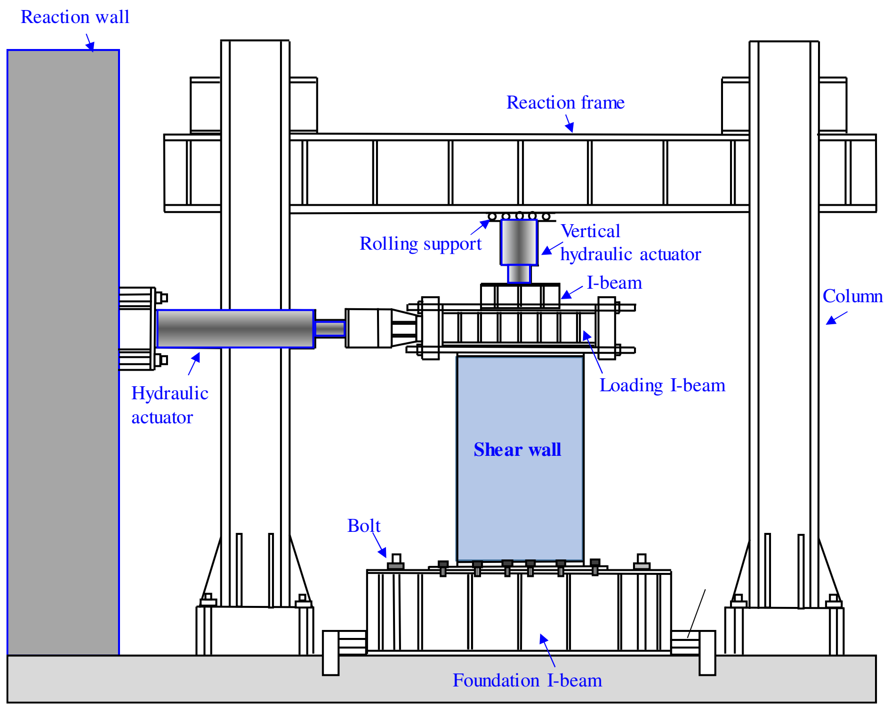

(b) Plane view of test setup

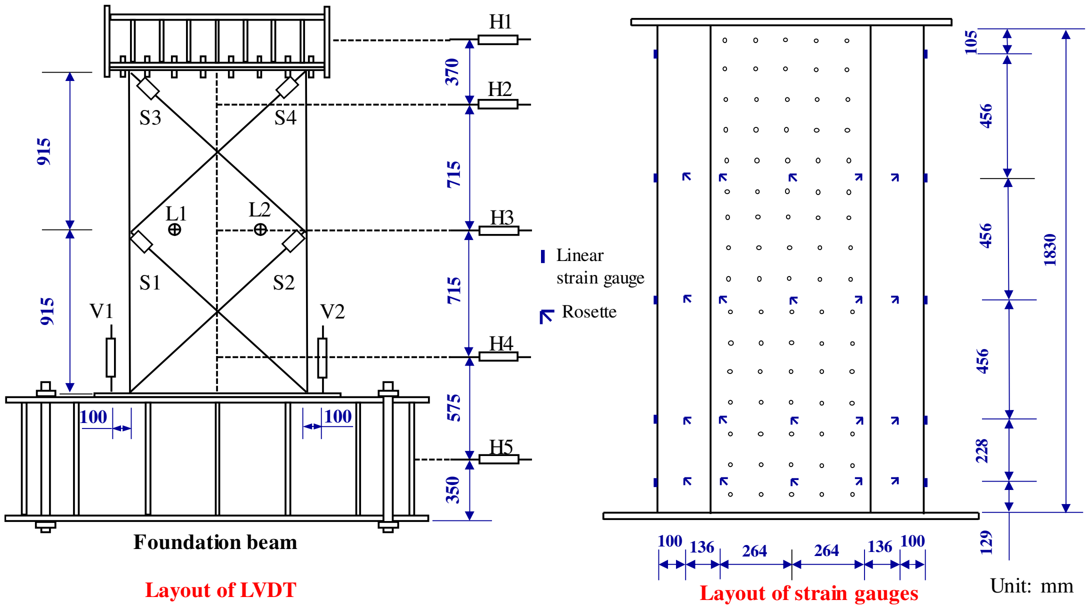

(c) Layout of LVDTs and strain gauges

Fig. 6 Test setup

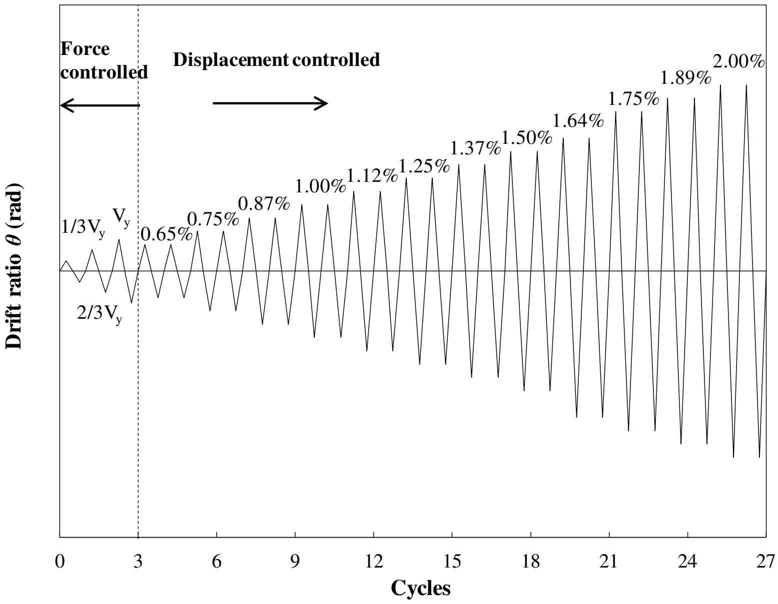

Fig. 7 Cyclic loading protocol

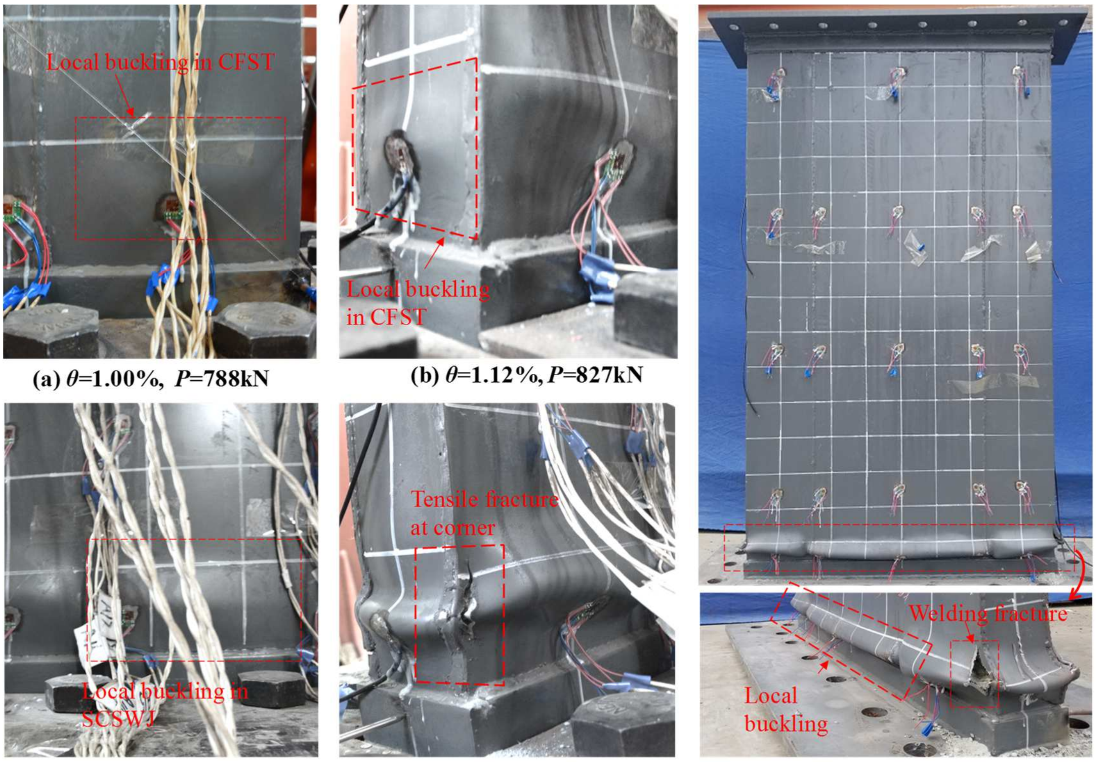

(a) θ=1.00%, P=788kN

(b) θ=1.12%, P=827kN

(c) θ=1.5%, P=809kN

(d) θ=1.64%, P=689kN

(e) θ=1.89%, P=616kN

Fig. 8 Failure modes of WBJ1

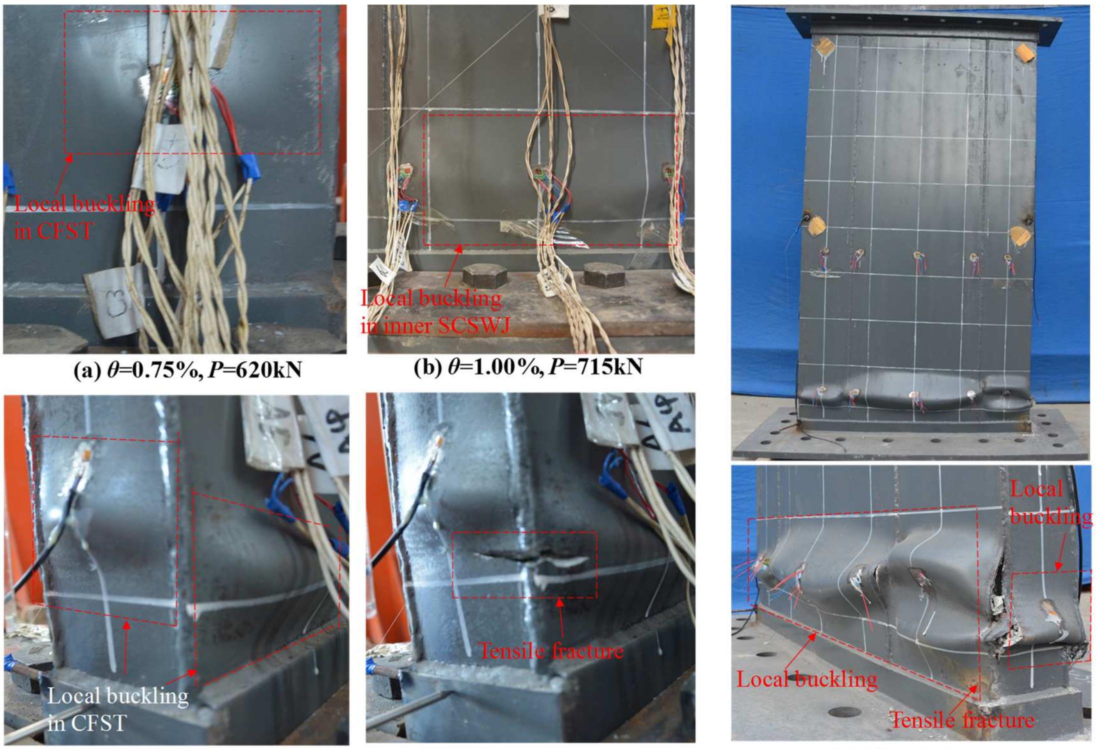

(a) θ=0.75%, P=620kN **(b) θ=1.00%, P=715kN**

(c) θ=1.00% P=715kN **(d) θ=1.25% P=737kN** **(e) After test**

Fig. 9 Failure modes of WBJ2

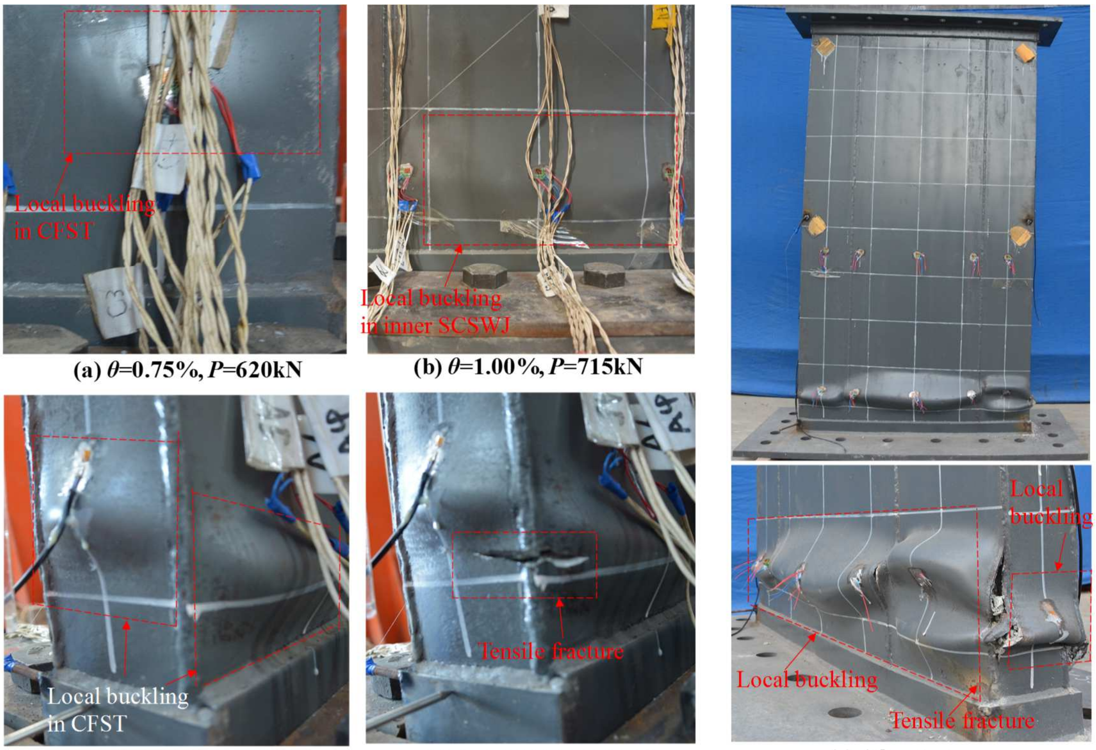

(a) θ=0.75%, P=620kN **(b) θ=1.00%, P=715kN**

(c) θ=1.00% P=715kN **(d) θ=1.25% P=737kN** **(e) After test**

Fig. 10 Failure modes of WBJ3

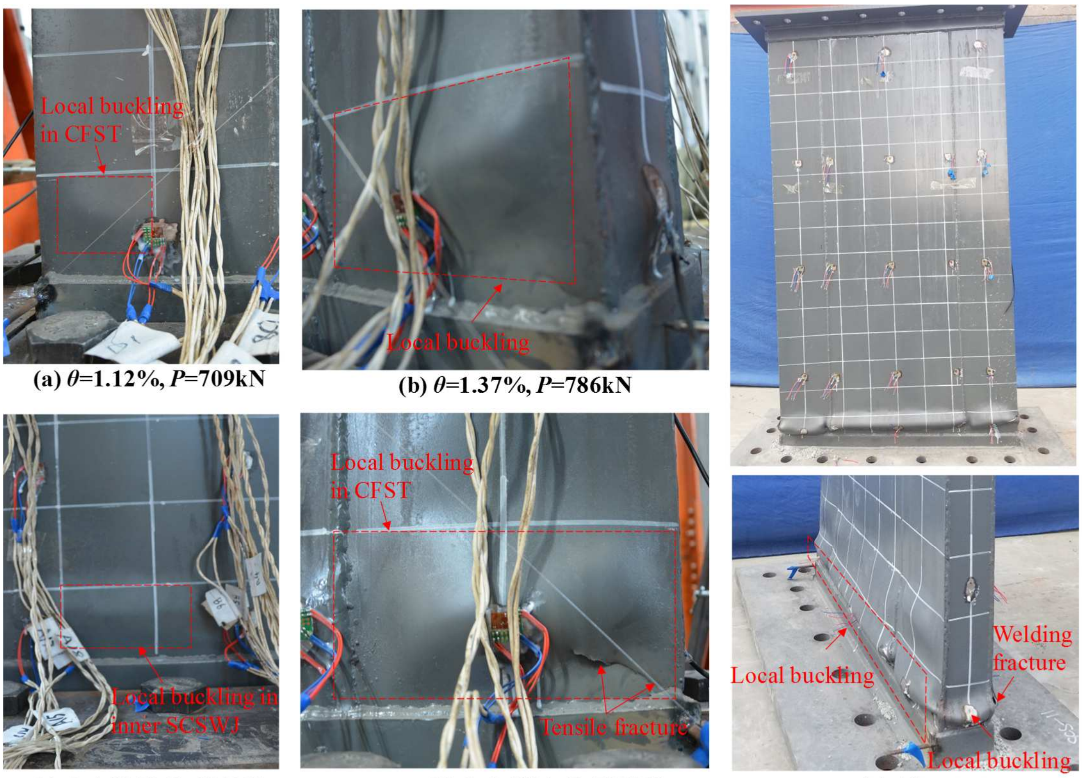

(a) θ**=1.12%,** P**=709kN** **(b)** θ**=1.37%,** P**=786kN**

(c) θ**=1.52%,** P**=800kN** **(d)** θ**=1.65%,** P**=793kN** **(e) After test**

Fig. 11 Failure modes of WBJ4

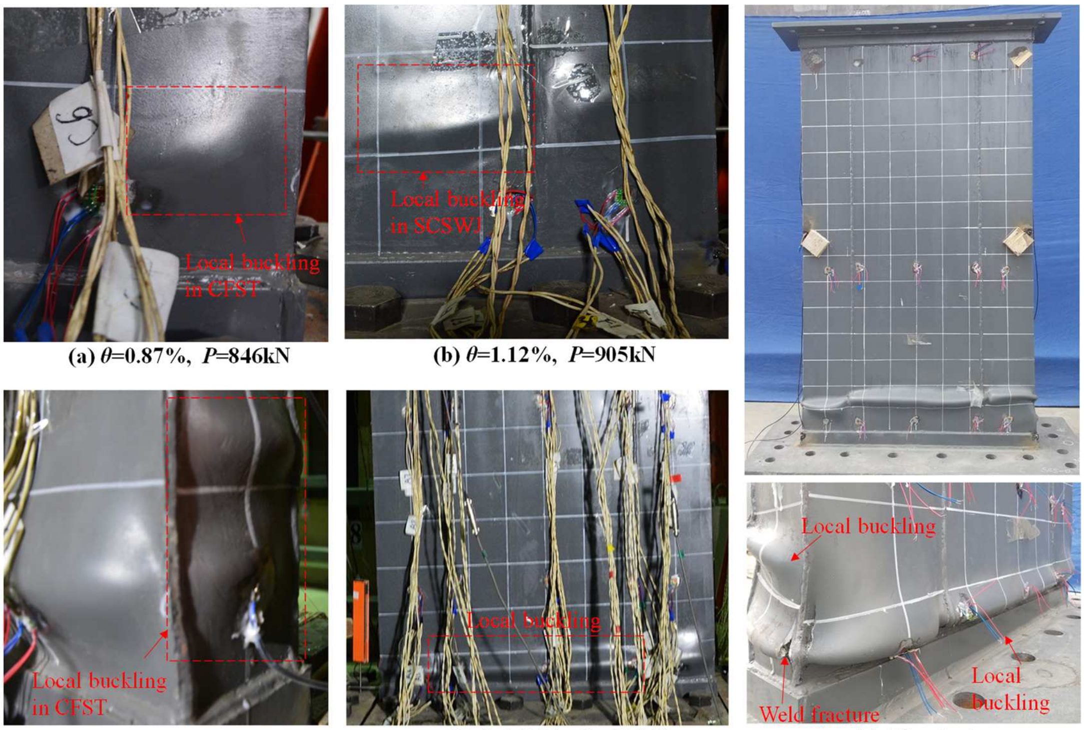

(a) θ**=0.87%,** P**=846kN** **(b)** θ**=1.12%,** P**=905kN**

(c) θ**=1.37%,** P**=926kN** **(d)** θ**=1.37%,** P**=644kN** **(e) After test**

Fig. 12 Failure modes of WBJ5

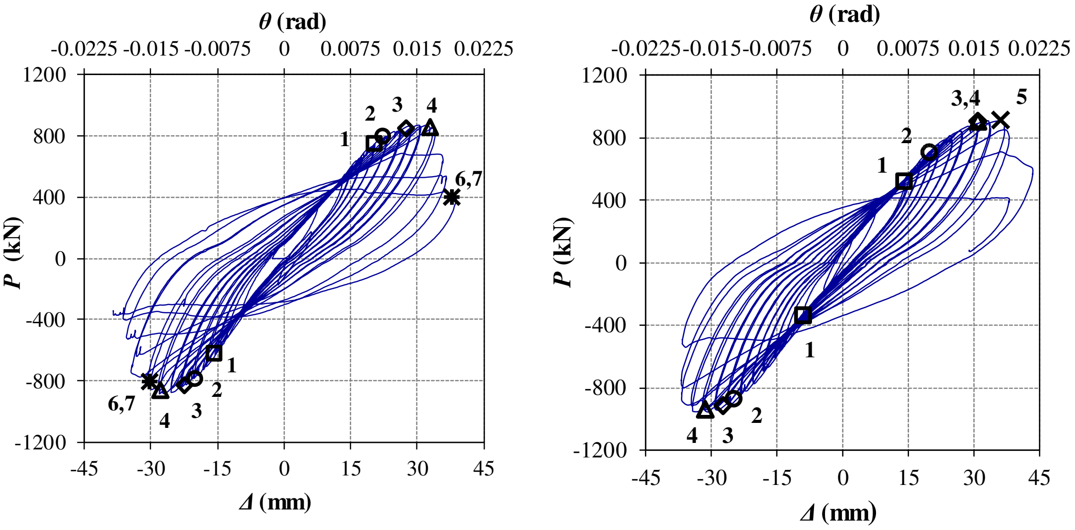

(a) WBJ1

(b) WBJ2

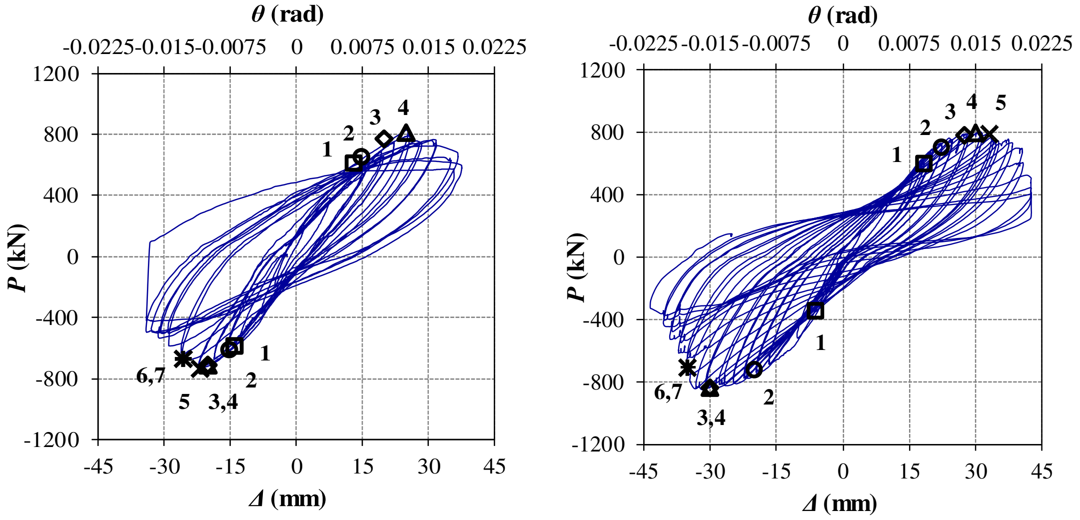

(c) WBJ3

(d) WBJ4

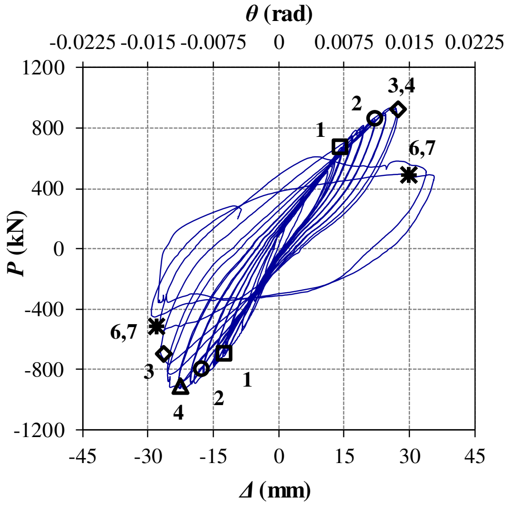

Notes:

1	□	Steel yielding
2	○	Local buckling of longer plate in CFST
3	◇	Local buckling of exterior shorter plate in CFST
4	△	Local buckling of steel faceplate in SCSWJ
5	×	Tensile fracture of steel plate in CFST
6	⚹	Tensile fracture of welding at corner
7	+	Concrete crushing

(e) WBJ5

Fig. 13 Hysteretic load versus top displacement curves

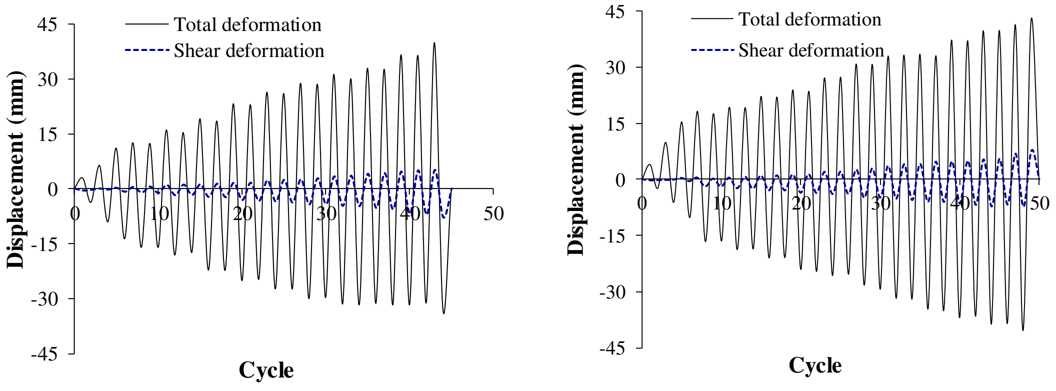

(a) WBJ1 (b) WBJ4

Fig. 14 Comparison between the shear deformation and total deformation

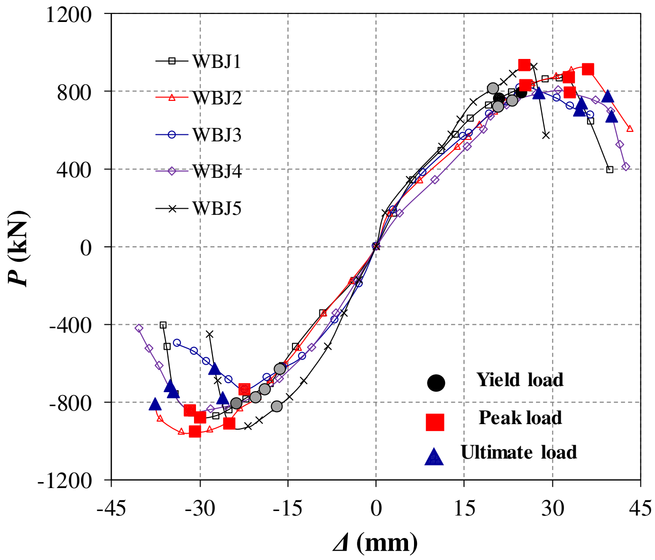

Fig. 15 Skeleton load-displacement curves

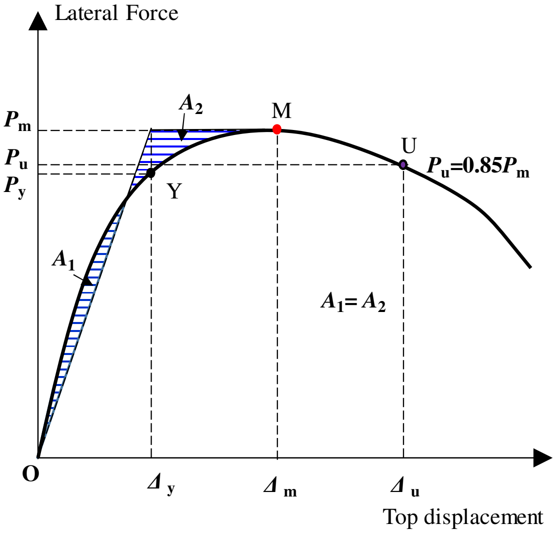

Fig. 16 Determinations of yield, peak and ultimate points in envelope curves

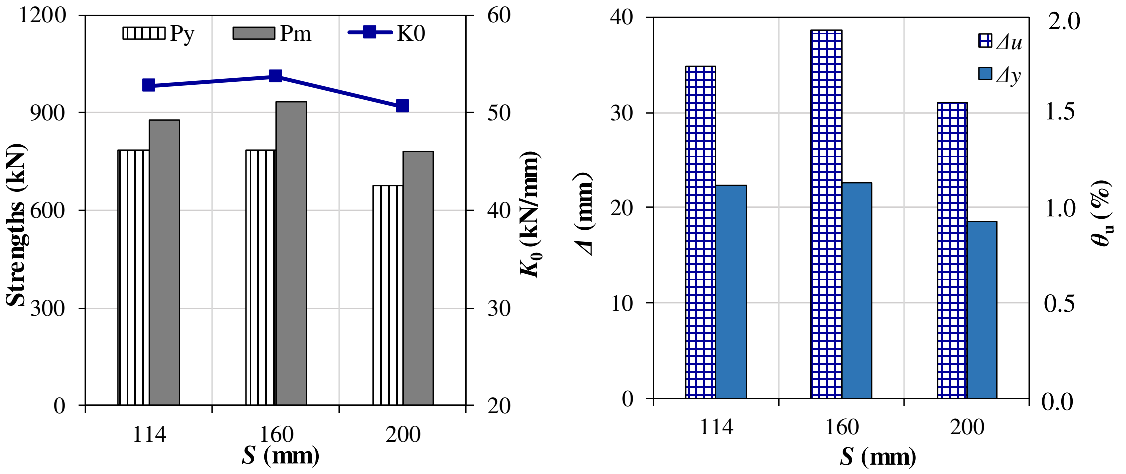

(a) Influence of *S* on strength

(b) Influence of *S* on Δ_y and Δ_u

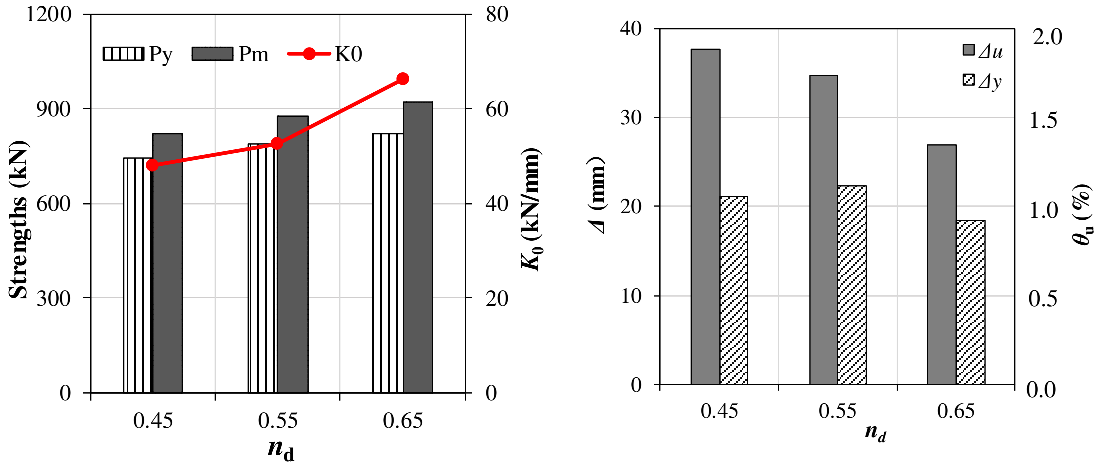

(c) Influence of n_d on strength

(d) Influence of n_d on Δ_y and Δ_u

Fig. 17 Influences of different parameters on strengths and ultimate displacement of SCSSWJ

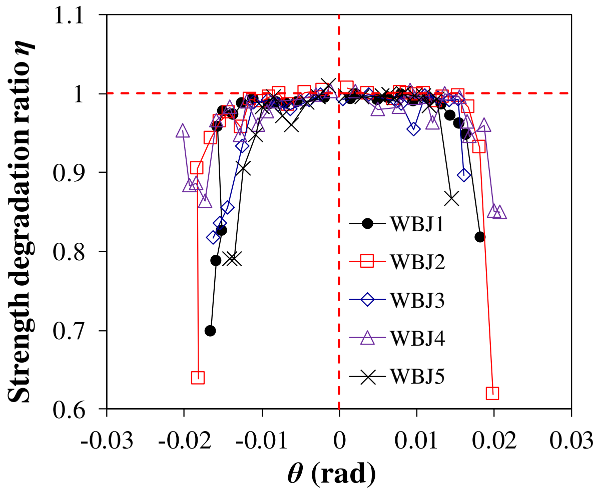

Fig. 18 Strength degradation versus drift angle curves of SCSSWJ

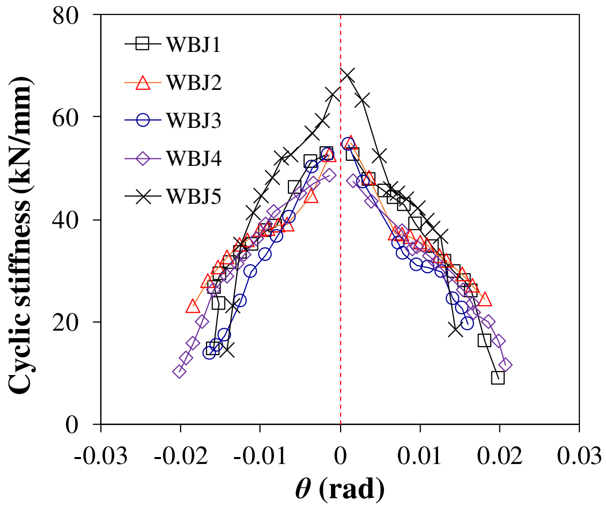

Fig. 19 Lateral stiffness versus drift angle curves of SCSSWJ

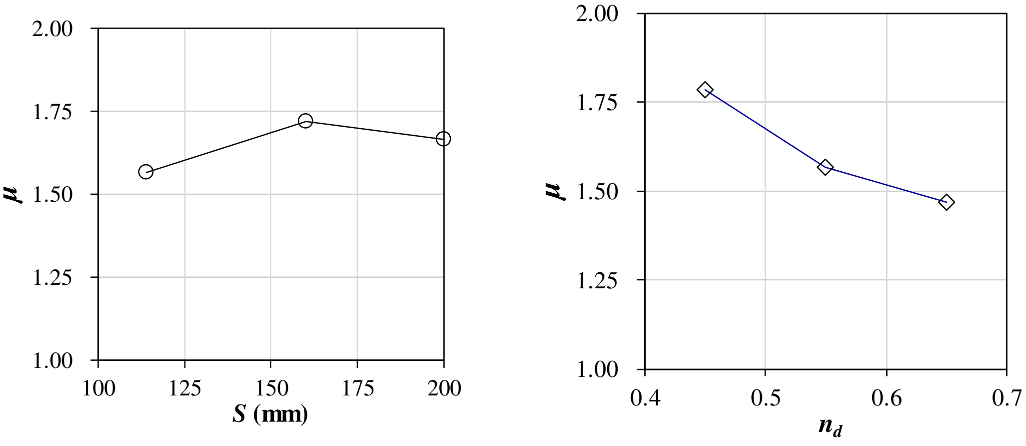

(c) Influence of S on μ

(d) Influence of n_d on μ

Fig. 20 Influences of S and n_d on ductility ratio

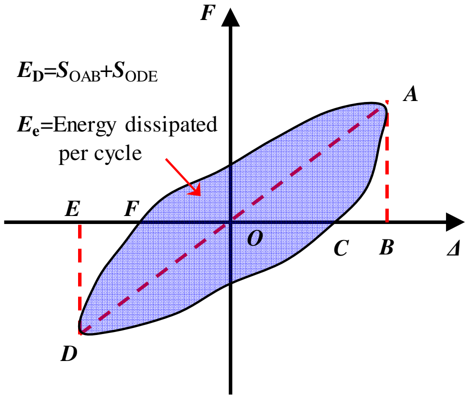

Fig. 21 Definition of energy dissipation

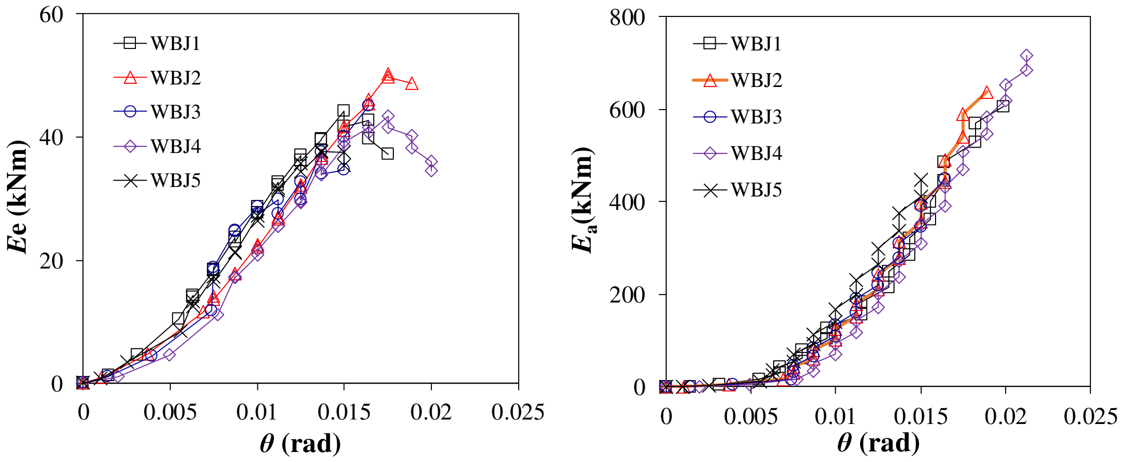

(a) Energy dissipated for each loading cycle

(b) Accumulated dissipated energy

Fig. 22 Energy dissipated of each loading cycle and accumulated dissipated energy versus drift angle curves of WBJ1~5

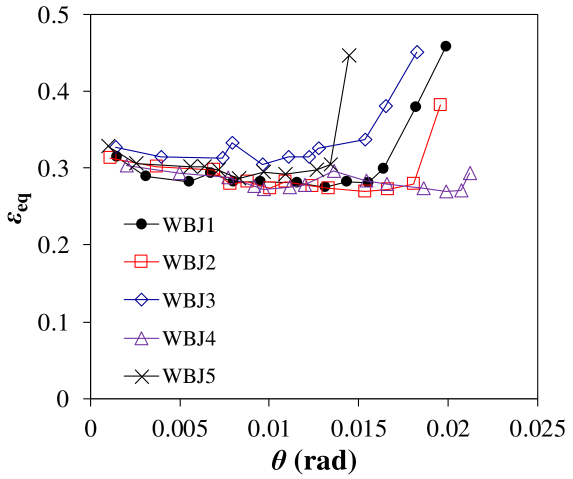

Fig. 23 Equivalent viscous damping coefficient of WBJ1~5

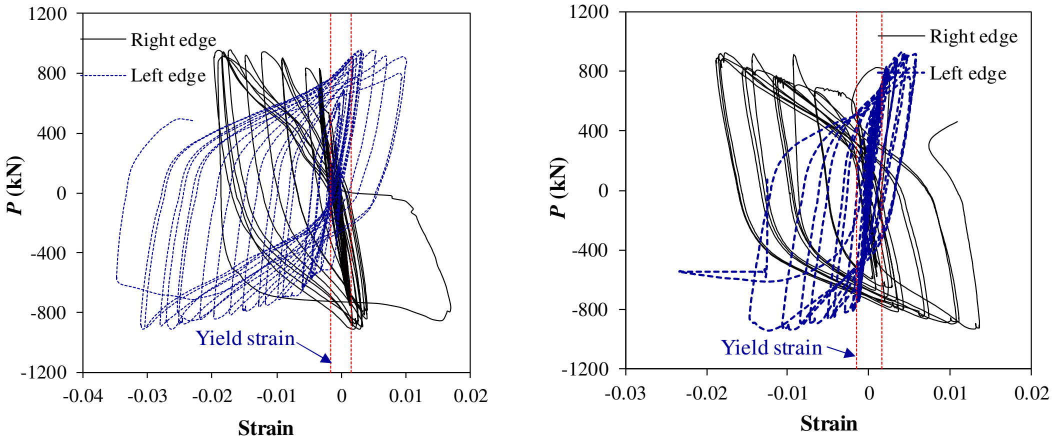

(a) WBJ2

(d) WBJ5

Fig. 24 Hysteretic load versus strain curves of the CFST column

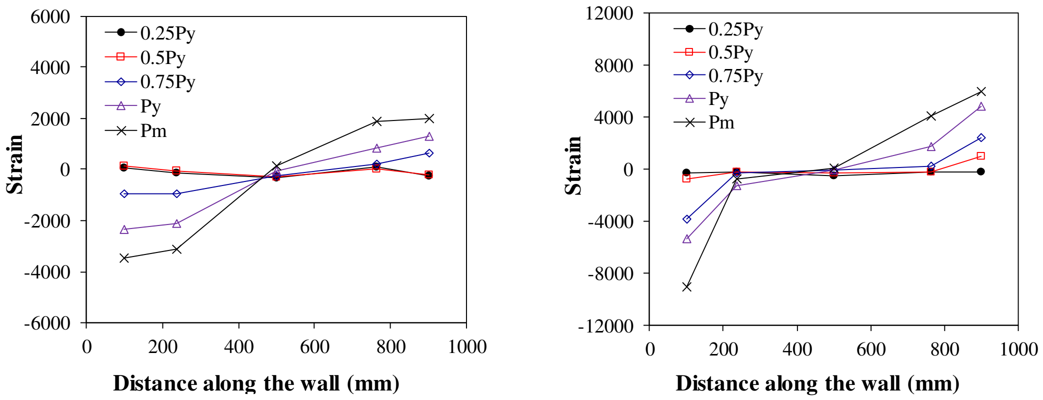

(a) WBJ1 (b) WBJ2

Fig. 25 Strain profile of the measured bottom cross section of the SCSSWJ

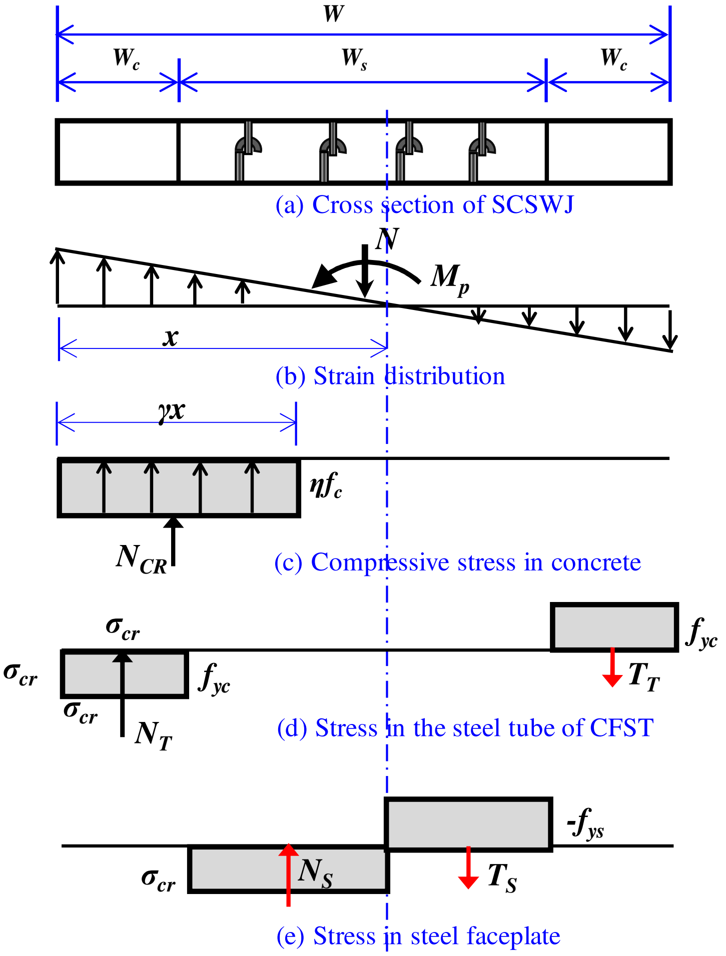

(a) Cross section of SCSWJ

(b) Strain distribution

(c) Compressive stress in concrete

(d) Stress in the steel tube of CFST

(e) Stress in steel faceplate

Fig. 26 Distribution of stress and cross-sectional flexural resistance of SCSSWJ

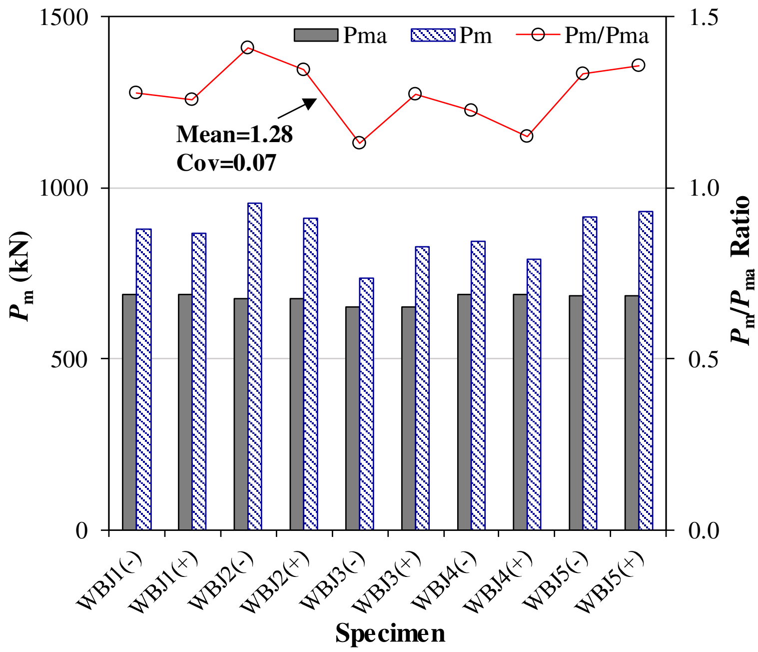

Fig. 26 Compression of ultimate lateral load carrying capacity between predictions and tests of SCSSWJ